




Dust dynamics in AGN winds: a new mechanism for multiwavelength AGN variability

Nadine H. Soliman   and Philip F. Hopkins 

TAPIR, Mailcode 350-17, California Institute of Technology, Pasadena, CA 91125, USA

Accepted 2023 August 9. Received 2023 August 2; in original form 2022 October 21

ABSTRACT

Partial dust obscuration in active galactic nuclei (AGNs) has been proposed as a potential explanation for some cases of AGN variability. The dust–gas mixture present in AGN tori is accelerated by radiation pressure, leading to the launching of an AGN wind. Dust under these conditions has been shown to be unstable to a generic class of fast-growing resonant drag instabilities (RDIs). In this work, we present the first numerical simulations of radiation-driven outflows that explicitly include dust dynamics in conditions resembling AGN winds. We investigate the implications of RDIs on the torus morphology, AGN variability, and the ability of radiation to effectively launch a wind. We find that the RDIs rapidly develop, reaching saturation at times much shorter than the global time-scales of the outflows, resulting in the formation of filamentary structure on box-size scales with strong dust clumping and super-Alfvénic velocity dispersions. The instabilities lead to fluctuations in dust opacity and gas column density of 10–20 per cent when integrated along mock observed lines of sight to the quasar accretion disc. These fluctuations occur over year to decade time-scales and exhibit a red-noise power spectrum commonly observed for AGNs. Additionally, we find that the radiation effectively couples with the dust–gas mixture, launching highly supersonic winds that entrain 70–90 per cent of the gas, with a factor of $\lesssim 3$ photon momentum loss relative to the predicted multiple-scattering momentum loading rate. Therefore, our findings suggest that RDIs play an important role in driving the clumpy nature of AGN tori and generating AGN variability consistent with observations.

Key words: instabilities – turbulence – dust, extinction – ISM: kinematics and dynamics – galaxies: formation.

1 INTRODUCTION

Dust plays a critical role in how a wide range of astrophysical systems form, evolve, and are observed. It is involved in processes such as planetary formation and evolution (Lissauer 1993; Apai & Loretta 2010; Liu & Ji 2020), chemical evolution (Whittet, Millar & Williams 1993; Weingartner & Draine 2001b; Watanabe & Kouchi 2008; Minissale et al. 2016), heating and cooling within the interstellar medium (ISM), and star formation (Salpeter 1977; Weingartner & Draine 2001a; Dorschner 2003; Draine 2003; Spitzer Jr 2008), as well as feedback and outflow launching in star-forming regions, cool stars, and active galactic nuclei (AGNs) (Murray, Quataert & Thompson 2005; King & Pounds 2015; Höfner & Olofsson 2018). Moreover, dust imprints ubiquitous observable signatures, such as the attenuation and extinction of observed light (Savage & Mathis 1979; Draine & Lee 1984; Mathis 1990).

One particular regime where dust is believed to play a central role in both dynamics and observations is the ‘dusty torus’ region around AGNs (Antonucci 1982; Lawrence & Elvis 1982; Urry & Padovani 1995; Choi et al. 2022). It is well established that outside of the dust sublimation radius, AGNs and quasars are surrounded by a dust-laden region with extinction and column densities ranging from $\sim 10^{22} \text{ cm}^{-2}$ in the polar direction to $\sim 10^{26} \text{ cm}^{-2}$ in the mid-plane (on average), exhibiting ‘clumpy’ substructure in both dust and

gas, ubiquitous time variability on $\gtrsim \text{yr}$ time-scales, and a diverse array of detailed geometric and reddening properties (see Krolik & Begelman 1988; Elitzur & Shlosman 2006; Tristram et al. 2007; Nenkova et al. 2008a, b; Stalevski et al. 2012; Leighly et al. 2015, or for recent reviews see Netzer 2015; Padovani et al. 2017; Baloković et al. 2018; Hickox & Alexander 2018), as well as a broad variety of different extinction curve shapes (Laor & Draine 1993; Hopkins et al. 2004; Maiolino et al. 2004; Hatziminaoglou, Fritz & Jarrett 2009; Gallerani et al. 2010; Höfner & Kishimoto 2010). It has been recognized for decades that the torus represents one of several natural locations where bright AGNs should drive outflows, and indeed many have gone so far as to propose the ‘torus’ is itself an outflow (see e.g. Sanders et al. 1988; Pier & Krolik 1992; Konigl & Kartje 1994; Elvis 2000; Elitzur & Shlosman 2006). Put simply, because the dust cross-section to radiation scattering and absorption is generally much larger than the Thompson cross section, which defines the Eddington limit, any AGN accreting at even modest fractions of Eddington should be able to unbind material via radiation pressure on dust, launching strong outflows. This concept has led to an enormous body of detailed observational follow-up (Horst et al. 2008; Bianchi et al. 2009; Tristram et al. 2009a; Höfner & Kishimoto 2010; Alonso-Herrero et al. 2011; Kishimoto et al. 2011a; Ricci et al. 2017; Höfner 2019) and detailed theoretical simulations and models of dust-radiation pressure-driven outflows from AGNs in the torus region (Thompson, Quataert & Murray 2005; Wada, Papadopoulos & Spaans 2009; Debuhr et al. 2010; Roth et al. 2012; Wada 2012; Ishibashi & Fabian 2015; Thompson et al. 2015; Chan & Krolik 2016; Baskin &

* E-mail: nsoliman@caltech.edu

Laor 2018; Costa et al. 2018; Ishibashi, Fabian & Maiolino 2018; Kawakatu, Wada & Ichikawa 2020; Venanzi, Hönig & Williamson 2020).

Yet, despite this extensive literature, almost all the theoretical work discussed above has assumed that the dust dynamics are perfectly coupled to the dynamics of the surrounding gas – effectively that the two ‘move together’ and the dust (even as it is created or destroyed) can simply be treated as some ‘additional opacity’ of the gas. But in reality, radiation absorbed/scattered by grains accelerates those grains, which then interact with gas via a combination of electromagnetic (Lorentz, Coulomb) and collisional (drag) forces, re-distributing that momentum.

Accurately accounting for these interactions is crucial for understanding any radiation-dust-driven outflows. If the dust ‘free-streaming length’ is very large, grains could simply be expelled before sharing their momentum with gas (Elvis, Marengo & Karovska 2002). If dust can be pushed into channels, creating low-opacity sight-lines through which radiation can leak out efficiently, some authors have argued that the coupled photon momentum might be far smaller than the standard expectation $\sim \tau_{\text{IR}} L/c$ (where τ_{IR} is the infrared optical depth; see Krumholz & Thompson 2012 but also Kuiper et al. 2012; Wise et al. 2012; Tsang & Milosavljević 2015).

Perhaps most importantly, Squire & Hopkins (2018b) showed that radiation-dust-driven outflows are generically unstable to a class of ‘resonant drag instabilities’ (RDIs). RDIs occur due to differences in the forces acting on the dust versus the gas and are inherently unstable across a broad range of wavelengths. However, the fastest growing modes, ‘resonant modes’, arise when the natural frequency of a dust mode matches that of a gas mode. Each pair of resonant modes leads to a unique instability with a characteristic growth rate, resonance, and mode structure. In subsequent works (Hopkins & Squire 2018a, b; Squire & Hopkins 2018a), the authors showed that systems like radiation-dust-driven outflows are unstable to the RDIs on all wavelengths – even scales much larger than the dust free-streaming length or mean free path. Subsequent idealized simulations of these instabilities (Hopkins & Squire 2018a; Moseley, Squire & Hopkins 2019; Seligman et al. 2019, Hopkins & Squire 2019a) have shown that they can grow rapidly, reaching significant non-linear amplitudes on large scales. Furthermore, the simulations demonstrated time-dependent clustering in both dust and gas, and a separation of dust and gas that is dependent on grain size. Additionally, the RDIs could drive fluctuations in the local dust-to-gas ratios which would affect the absorption and re-emission of radiation at different wavelengths. Specifically, as dust dominates the variability in the optical-UV bands but has a weaker effect on the IR and X-ray bands, dust-to-gas fluctuations can result in differences in the observed variability of the AGN emission across the electromagnetic spectrum.

The insights gained from these simulations are crucial not only for determining the initiation of an outflow but also for explaining various related phenomena. These include clumping in the torus, variations in AGN extinction curves, and specific forms of temporal variability. AGN sources are known to exhibit variability at essentially all wavelengths and time-scales, ranging from hours to billions of years (Paolillo et al. 2004, 2017; Uttley & McHardy 2004; Caplar, Lilly & Trakhtenbrot 2017; Assef et al. 2018). However, there have been observations of sources where the X-ray flux varies by approximately 20 per cent to 80 per cent over a few years, with no apparent variation in the optical component (Risaliti, Elvis & Nicastro 2002; Risaliti et al. 2005; De Rosa et al. 2007; Smith & Vaughan 2007; Markowitz, Krumpke & Nikutta 2014; Laha et al. 2020). In some cases, ‘changing-look’ AGNs have shown order of

magnitude variability on time-scales as short as a few days to a couple hours (e.g. LaMassa et al. 2015; McElroy et al. 2016; Ruan et al. 2016; Runnoe et al. 2016; Mathur et al. 2018; Stern et al. 2018; Wang, Xu & Wei 2018; Yang et al. 2018; Trakhtenbrot et al. 2019; Hon, Webster & Wolf 2020; Ross et al. 2020). However, the processes driving such variability and the clumpy nature of the torus remain unexplained.

In this study, we investigate the behaviour of radiation-dust-driven outflows for AGN tori, including explicit dust–gas radiation dynamics for the first time. We introduce our numerical methods and initial conditions in Section 2, followed by an analysis of our results in Section 4. We analyse the morphology, dynamics, and non-linear evolution of the dusty gas in the simulations, and in Section 4.2 we compare our standard simulations results to simulations with full radiation-dust-magnetohydrodynamics (RDMHD). Additionally, we investigate the feasibility of launching radiation-driven outflows and measure the momentum coupling efficiency within the wind in Section 4.3. In Section 5.1, we examine how the presence of RDIs affects observable AGN properties, such as time variability. Finally, we provide a summary of our findings in Section 6.

2 METHODS AND PARAMETERS

We consider an initially vertically stratified mixture of magnetized gas (obeying the ideal MHD equations) and an observationally motivated spectrum of dust grains with varying size, mass, and charge. The dust and gas are coupled to one another via a combination of electromagnetic and collisional/drag forces. The system is subject to an external gravitational field, and the dust absorbs and scatters radiation from an external source. In Fig. 1, we show a cartoon illustrating the geometry of our idealized set-up and its relation to an AGN torus.

2.1 Numerical methods

The numerical methods for our simulations are identical to those in Hopkins et al. (2022), to which we refer for more details (see also Hopkins & Lee 2016; Lee, Hopkins & Squire 2017; Moseley et al. 2019; Seligman, Hopkins & Squire ; Hopkins, Squire & Seligman 2020b; Ji, Squire & Hopkins 2022; Steinwandel et al. 2022; Squire, Moroianu & Hopkins 2022 for additional details and applications of these methods). Briefly, we run our simulations with the code GIZMO¹ (Hopkins 2015), utilizing the Lagrangian ‘meshless finite mass method’ to solve the equations of ideal MHD (Hopkins 2016, 2017; Hopkins & Raives 2016; Su et al. 2017). Dust grains are modelled as ‘superparticles’ (Carballido, Stone & Turner 2008; Johansen, Youdin & Mac Low 2009; Bai & Stone 2010; Pan et al. 2011; McKinnon et al. 2018) where each simulated ‘dust particle’ represents an ensemble of dust grains with a similar grain size (ϵ_{grain}), charge (q_{grain}), and mass (m_{grain}).

We simulate a 3D box with a base of length $H_{\text{gas}} = L_{xy}$ in the xy plane and periodic \hat{x} , \hat{y} boundaries, and height $L_{\text{box}} = L_z = 20 L_{xy}$ in the \hat{z} direction with a reflecting lower ($z = 0$) and outflow upper ($z = +L_z$) boundary. Dust and gas feel a uniform external gravitational field $\mathbf{g} = -g \hat{z}$. The gas has initial uniform velocity $\mathbf{u}_g^0 = 0$, initial magnetic field $\mathbf{B}_0 \equiv B_0 \hat{\mathbf{B}}_0$ in the xz plane ($\hat{\mathbf{B}}_0 = \sin(\theta_B^0) \hat{x} + \cos(\theta_B^0) \hat{z}$), obeys a strictly isothermal equation of

¹A public version of the code is available at http://www.tapir.caltech.edu/~p_hopkins/Site/GIZMO.html

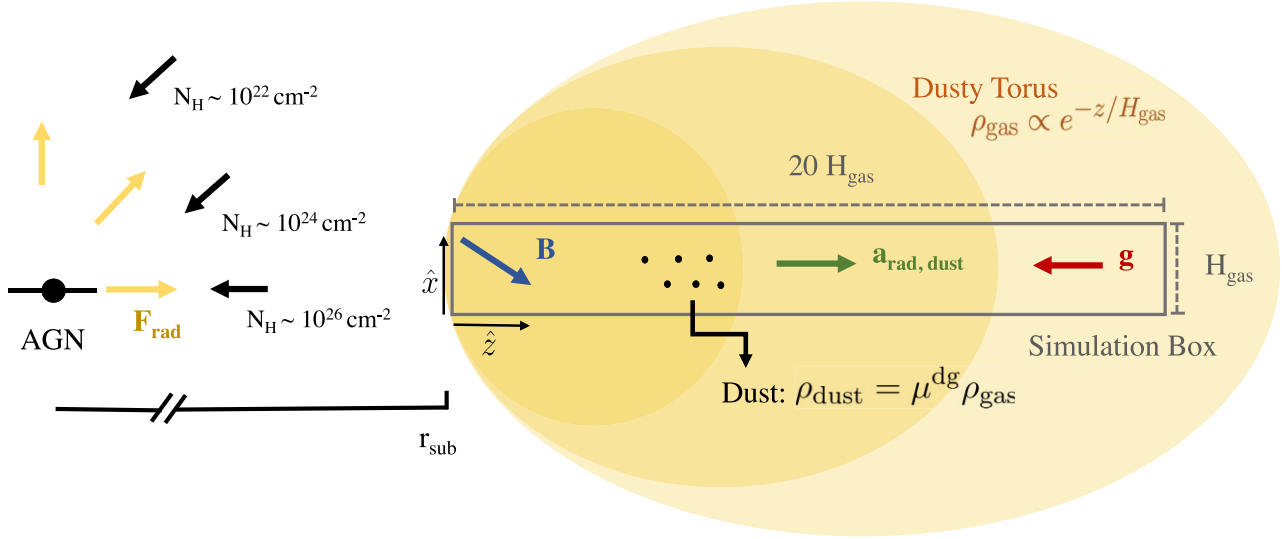


Figure 1. Cartoon illustrating our simulation set-up. We simulate 3D boxes of size $H_{\text{gas}} \times H_{\text{gas}} \times 20 H_{\text{gas}}$ along the \hat{x} , \hat{y} , and \hat{z} directions, respectively, with $\sim 10^6$ resolution elements. We enforce outflow upper and reflecting lower boundary conditions with periodic sides. The gas and dust are initially stratified such that $\rho_{\text{gas}} \propto e^{-z/H_{\text{gas}}}$, and $\rho_{\text{d}} = \mu_0^{\text{dg}} \rho_{\text{gas}}$, where $\mu_0^{\text{dg}} = 0.01$ corresponding to a uniform dust-to-gas ratio. The gas follows an isothermal ($\gamma = 1$) EOS with sound speed c_s , an initial magnetic field $\mathbf{B}_0 = |\mathbf{B}|(\sin\theta_B^0 \hat{x} + \cos\theta_B^0 \hat{z})$ in the $\hat{x} - \hat{z}$ plane, and gravitational acceleration $\mathbf{g} = -g\hat{z}$. The dust grains are modelled as superparticles each representing a population of grains of a given size sampled from a standard MRN spectrum with a factor = 100 range of sizes. The grains are photoelectrically charged, with the charge appropriately scaled according to grain size. They experience an upward acceleration $\mathbf{a}_{\text{rad,dust}}$ due to absorption of an initial upward radiation flux $F_0 = +F_0\hat{z}$ corresponding to radiation from an AGN located a sublimation radius r_{sub} distance away, and are coupled to the gas through drag and Lorentz forces. We consider a range of 10^{22} – 10^{26} cm^{-2} in column densities representing different lines-of-sight angles through the dusty torus.

state ($P = \rho_g c_s^2$), and the initial gas density is stratified with $\rho_g^0 \equiv \rho_g(t=0) = \rho_{\text{base}} \exp(-z/H_{\text{gas}})$ (with $\rho_{\text{base}} \approx M_{\text{gas, box}}/H_{\text{gas}}^3$).

Each dust grain obeys an equation of motion

$$\begin{aligned} \frac{d\mathbf{v}_d}{dt} &= \mathbf{a}_{\text{gas,dust}} + \mathbf{a}_{\text{grav}} + \mathbf{a}_{\text{rad}} \\ &= -\frac{\mathbf{w}_s}{t_s} - \frac{\mathbf{w}_s \times \hat{\mathbf{B}}}{t_L} + \mathbf{g} + \frac{\pi \epsilon_{\text{grain}}^2}{m_{\text{grain}} c} \langle Q \rangle_{\text{ext}} \mathbf{G}_{\text{rad}}, \end{aligned} \quad (1)$$

where \mathbf{v}_d is the grain velocity; $\mathbf{w}_s \equiv \mathbf{v}_d - \mathbf{u}_g$ is the drift velocity for a dust grain with velocity \mathbf{v}_d and gas velocity \mathbf{u}_g at the same position \mathbf{x} ; \mathbf{B} is the local magnetic field; $\mathbf{a}_{\text{gas,dust}} = -\mathbf{w}_s/t_s - \mathbf{w}_s \times \hat{\mathbf{B}}/t_L$ includes the forces from gas on dust including drag (in terms of the ‘stopping time’ t_s) and Lorentz forces (with gyro/Larmor time t_L); $\mathbf{a}_{\text{grav}} = \mathbf{g}$ is the external gravitational force; and \mathbf{a}_{rad} is the force from radiation in terms of the grain size ϵ_{grain} , mass $m_{\text{grain}} \equiv (4\pi/3) \bar{\rho}_{\text{grain}}^i \epsilon_{\text{grain}}^3$ (in terms of the internal grain density $\bar{\rho}_{\text{grain}}^i$), dimensionless absorption + scattering efficiency $\langle Q \rangle_{\text{ext}}$, speed of light c , and radiation field $\mathbf{G}_{\text{rad}} \equiv \mathbf{F}_{\text{rad}} - \mathbf{v}_d \cdot (e_{\text{rad}} \hat{\mathbf{I}} + \mathbb{P}_{\text{rad}})$ in terms of the radiation flux/energy density/pressure density \mathbf{F}_{rad} , e_{rad} , \mathbb{P}_{rad} . The dust is initialized with the local homogeneous steady-state equilibrium drift and a spatially uniform dust-to-gas ratio $\rho_d^0 = \mu^{\text{dg}} \rho_g^0$. For all forces ‘from gas on dust’ $\mathbf{a}_{\text{gas,dust}}$ the gas feels an equal-and-opposite force (back-reaction). The dust gyro time is given in terms of the grain charge $q_{\text{grain}} = Z_{\text{grain}} e$ as $t_L \equiv m_{\text{grain}} c / |q_{\text{grain}} \mathbf{B}|$, and for the parameter space of our study the drag is given by Epstein drag (as opposed to Coulomb or Stokes drag) with

$$t_s \equiv \sqrt{\frac{\pi \gamma}{8} \frac{\bar{\rho}_{\text{grain}}^i \epsilon_{\text{grain}}}{\rho_g c_s}} \left(1 + \frac{9\pi \gamma}{128} \frac{|\mathbf{w}_s|^2}{c_s^2} \right)^{-1/2}. \quad (2)$$

We adopt a standard empirical Mathis, Rumpl & Nordsieck (1977) power-law grain size spectrum with differential num-

ber $dN_d/d\epsilon_{\text{grain}} \propto \epsilon_{\text{grain}}^{-3.5}$ with a range of a factor of 100 in grain size ($\epsilon_{\text{grain}}^{\text{max}} = 100 \epsilon_{\text{grain}}^{\text{min}}$). We assume the grain internal density/composition is independent of grain size, and assume the charge-to-mass ratio scales as $|q_{\text{grain}}|/m_{\text{grain}} \propto \epsilon_{\text{grain}}^{-2}$, consistent with grains charged by a range of processes relevant in this regime such as collisions, Coulomb, photoelectric, or electrostatically limited processes (Draine & Sutin 1987; Tielens 2005).

As in Hopkins et al. (2022), we consider two different treatments of the radiation fields. Given the range of column densities we will explore, we are interested in the multiple-scattering regime, or equivalently Rayleigh scattering. In this regime, the radiation should be in the long-wavelength limit (spectrum peaked at wavelengths $\lambda_{\text{rad}} \gg \epsilon_{\text{grain}}$), so we expect and assume the spectrally averaged $\langle Q \rangle_{\text{ext}} \propto \epsilon_{\text{grain}}$, and we approximate the radiation with a single band (spectrally integrated), so effectively treat the grains as introducing a grain-size-dependent but otherwise ‘grey’ isotropic scattering opacity. In our first simplified treatment (our ‘constant flux’ simulations), we assume the radiation fields obey their homogeneous equilibrium solution, giving $\mathbf{G}_{\text{rad}} \approx \mathbf{F}_{\text{rad}} \approx \mathbf{F}_0 = F_0 \hat{z}$. This is a reasonable approximation so long as the radiation is not ‘trapped’ in highly inhomogeneous dust clumps. But we also run a subset of RDMHD simulations where the radiation field is explicitly evolved using the full M1 radiation-hydrodynamics treatment in GIZMO (Lupi, Volonteri & Silk 2017; Lupi et al. 2018; Hopkins & Grudić 2019; Hopkins et al. 2020a; Grudić et al. 2021), including terms to $\mathcal{O}(v^2/c^2)$: $\partial_t e_{\text{rad}} + \nabla \cdot \mathbf{F}_{\text{rad}} = -R_{\text{dust}} \mathbf{v}_d \cdot \mathbf{G}_{\text{rad}}/c^2$, $\partial_t \mathbf{F}_{\text{rad}} + c^2 \nabla \cdot \mathbb{P}_{\text{rad}} = -R_{\text{dust}} \mathbf{G}_{\text{rad}}$, where the absorption/scattering coefficients R_{dust} are calculated directly from the explicitly resolved dust grain populations (consistent exactly with the radiation flux they see in \mathbf{a}_{rad}).

Our default simulation parameter survey adopts 10^6 gas cells and 4×10^6 dust superparticles. And unless otherwise specified, our

analysis uses the ‘full RDMHD’ simulations. Readers interested in details should see Hopkins et al. (2022). In that paper, we applied these numerical methods to simulations of radiation-dust-driven outflows in molecular clouds and H II regions. The key differences are (1) we consider a very different parameter space (much higher densities and stronger radiation fields), which lead to qualitatively different instabilities and behaviours, and (2) we specifically model the multiple-scattering regime, while Hopkins et al. (2022) focused only on the single-scattering limit.

2.2 Parameter choices

Our simulations are then specified by a set of constants (size and charge of the largest grains, dust-to-gas ratio, radiation flux, etc.). To motivate these, we consider a fiducial case of dust around a bright quasar. We expect the most dramatic effects of radiation on dust at the distances closest to the black hole (BH) where grains can survive, i.e. just outside the dust sublimation radius $r_{\text{sub}} \sim (L_{\text{QSO}}/4\pi\sigma_{\text{SB}}T_{\text{sub}}^4)^{1/2}$, where $T_{\text{sub}} \sim 2000$ K is the dust sublimation temperature and we will consider a typical quasar with $L_{\text{QSO}} \sim 10^{46}$ erg s $^{-1}$ (i.e. $M_{\text{B}} \sim -24$, a typical $\sim L_*$ or modestly sub- L_* QSO at redshifts $z \sim 1-6$; see Shen et al. 2020), so $r_{\text{sub}} \sim 0.3$ pc and this corresponds to a BH of mass $M_{\text{BH}} \sim 10^8 M_{\odot}$ accreting near its Eddington limit.

We then take $H_{\text{gas}} \sim r_{\text{sub}}$, $F_0 \sim L_{\text{QSO}}/(4\pi r_{\text{sub}}^2)$, $g \sim GM_{\text{BH}}/r_{\text{sub}}^2$, typical $\bar{\rho}_{\text{grain}}^i \sim 1.5$ g cm $^{-3}$ and absorption efficiency for the largest grains $\langle Q \rangle_{\text{ext}}(\epsilon_{\text{grain}} = \epsilon_{\text{grain}}^{\text{max}}) \sim 0.2$ (Draine & Lee 1984), and initial magnetic field strength given by a plasma $\beta_0 \equiv (c_s/v_A[z=0])^2 = 4\pi\rho_{\text{base}}(c_s/B_0)^2 \sim 1$ with an arbitrary angle $\theta_B^0 = \pi/4$ (though this is essentially a nuisance parameter here). Observational constraints suggest the dust-to-gas ratios integrated along AGN lines of site range from 0.01–1 times the galactic values (Maiolino et al. 2001; Burtcher et al. 2016; Esparza-Arredondo et al. 2021). However, these measurements include regions within the dust sublimation radius and therefore should be interpreted as lower limits. Several studies suggest that the broad-line region has supersolar dust-to-gas ratios (Sturm et al. 2006; Nenkova et al. 2008b; Kishimoto, Hönig & Antonucci 2009). Therefore, given these uncertainties, we assume a standard (galactic) dust-to-gas ratio $\mu^{\text{dg}} = 0.01$. Further, we consider various values of $\epsilon_{\text{grain}}^{\text{max}}$ from 0.01 μm (smaller grains than typical in the diffuse ISM) through 1 μm (larger), and also explore variations in the gas density parametrized via the gas column density integrated through the box to infinity, $N_{\text{H,gas}} \equiv m_p^{-1} \int \rho_g^0 dz = \rho_{\text{base}} H_{\text{gas}}/m_p \sim 10^{22}-10^{26}$ cm $^{-2}$, representative of observed values through different lines of sight of angles through the AGN torus.

The one remaining parameter is the dust charge. We have considered both (a) cases where the grains are strongly shielded and the gas neutral/cold, so collisional charging dominates, and (b) cases where some photoelectric (non-ionizing UV) flux can reach the grains. Given the scalings for grain charge in both regimes (Draine & Sutin 1987; Tielens 2005), if even a small fraction of the QSO photoelectric flux reaches the grains, they will generally reach the electrostatic photoelectric charging limit such that the equilibrium grain charge $\langle Z_{\text{grain}} \rangle \sim 5000(\epsilon_{\text{grain}}/\mu\text{m})$ (Tielens 2005). For simplicity, we adopt this by default. However, we note that using the collisional charge expression from Draine & Sutin (1987), which results in a significant decrease in $|Z_{\text{grain}}|$, has little effect. This is because we find that in the parameter space of interest, the magnetic grain–gas interactions (grain charge effects) are sub-dominant, even with the larger $|Z_{\text{grain}}|$. In Appendix A, we provide a table that lists the specific parameters for each simulation.

3 ANALYTIC EXPECTATIONS AND BACKGROUND

Hopkins & Squire (2018b) analysed the equations of mass and momentum conservation using a linear stability approach to investigate the behaviour of an unstable RDI mode in a dust–gas mixture similar to those simulated in our study. They found that the behaviour of an unstable mode with wave-vector \mathbf{k} is characterized by the dimensionless parameter $\mathbf{k} \cdot \mathbf{w}_s \langle t_s \rangle$, where $\langle t_s \rangle = t_s(\langle \rho_g \rangle, \langle \mathbf{w}_s \rangle)$ corresponds to the stopping time at the equilibrium gas density $\langle \rho_g \rangle$ and equilibrium drift velocity $\langle \mathbf{w}_s \rangle$ of the dust particles. This parameter represents the ratio of the dust stopping length to the wavelength of the mode, and defines three regimes of the instabilities,

$$\begin{cases} \mathbf{k} \cdot \mathbf{w}_s \langle t_s \rangle \lesssim \mu^{\text{dg}} & \text{(Low-k, long-wavelength)} \\ \mu^{\text{dg}} \lesssim \mathbf{k} \cdot \mathbf{w}_s \langle t_s \rangle \lesssim (\mu^{\text{dg}})^{-1} & \text{(Mid-k, intermediate wavelength)} \\ \mathbf{k} \cdot \mathbf{w}_s \langle t_s \rangle \gtrsim (\mu^{\text{dg}})^{-1} & \text{(High-k, short-wavelength),} \end{cases} \quad (3)$$

separated by their linear growth rate scaling and mode structure. The different regimes can be further understood by considering the parameter $\mu^{\text{dg}} \mathbf{k} \cdot \mathbf{w}_s \langle t_s \rangle$, which can be interpreted as the ratio of the force exerted by the dust on the gas to the gas pressure forces for a given scale $|\mathbf{k}|$ (Moseley et al. 2019). The mid-k and high-k regimes exhibit similar behaviour and occur when the gas pressure dominates the dynamics on the scales being considered. Therefore, the resonant mode occurs when the drift velocity aligns with the propagation direction of the gas mode, as given by $\hat{\mathbf{k}} \cdot \mathbf{w}_s = \pm c_s$. On the other hand, the low-k regime arises when the bulk force exerted by the dust on the gas becomes stronger than the gas pressure forces, and the dust dominates the flow. Resonant modes in this regime typically align with \mathbf{w}_s .

As shown in equation (3), the dust-to-gas ratio plays an important role in distinguishing the different RDI regimes. However, for most of our simulations, transitioning into a different regime would require a significant adjustment of μ^{dg} by several orders of magnitude. Given the specific environmental conditions we aim to model and the likelihood of accurately representing the intended scenario while having such drastic variations in μ^{dg} , we choose to use our fiducial value for μ^{dg} in all simulations. For a study of the effect of varying μ^{dg} on the behaviour of the RDIs, we refer readers to Moseley et al. (2019).

Rewriting the regimes above in terms of wavelength, we can see that $\lambda_{\text{crit}} \sim (\bar{\rho}_{\text{grain}}^i \epsilon_{\text{grain}})/(\mu^{\text{dg}} \rho_g) \sim \tilde{\alpha} H_{\text{gas}}/\mu^{\text{dg}}$ defines the critical wavelength above which modes are in the low-k regime, where $\tilde{\alpha} \equiv (\bar{\rho}_{\text{grain}}^i \epsilon_{\text{grain}})/(\rho_{\text{base}} H_{\text{gas}})$ is the dimensionless grain size parameter which characterizes the coupling strength between the dust and gas. For the parameter set explored here, $\tilde{\alpha} \ll \mu^{\text{dg}}$, we find that largest wavelength interesting modes ($\lambda \sim H_{\text{gas}} \gg \lambda_{\text{crit}}$) always lie in the ‘long-wavelength’ regime. Within the linear theory framework, this mode behaves as a ‘compressible wave’, with similar dust and gas velocity perturbations that are nearly in phase and parallel to the wave-vector $\hat{\mathbf{k}}$. This will therefore drive relatively weak dust–gas separation with respect to other regimes previously studied in Hopkins et al. (2022). The linear growth time-scale t_{grow} of the fastest growing modes in this regime scales approximately as

$$t_{\text{grow}}(k) \sim \frac{1}{\mathfrak{F}(k)} \sim \left(\frac{\mu^{\text{dg}} \langle \mathbf{w}_s^2 \rangle k^2}{\langle t_s \rangle} \right)^{-1/3}, \quad (4)$$

where $\mathfrak{F}(k)$ is the linear growth rate for a mode with wavenumber k (Hopkins & Squire 2018b). Importantly, as shown therein, the fastest growing mode in the linear long-wavelength regime is the ‘pressure-

free' mode, which is weakly dependent on the magnetization and thermal physics of the gas. We discuss this further below.

We define the geometrical optical depth τ_{geo} instead of the 'observed' optical depth τ_λ since the latter depends on the observed wavelength (the same integral replacing $\pi\epsilon_{\text{grain}}^2 \rightarrow Q_\lambda(\epsilon_{\text{grain}}, \lambda)\pi\epsilon_{\text{grain}}^2$), integrated from the base of the box to infinity. Assuming a vertically stratified environment and dust grains with a power-law grain size spectrum, we can express τ_{geo} strictly in terms of our simulation parameters,

$$\begin{aligned} \tau_{\text{geo}} &\equiv \int_0^\infty \pi\epsilon^2 n_{\text{grain}} dz \\ &= C \mu^{\text{dg}} \frac{\rho_g H_{\text{gas}}}{\rho_d \epsilon_{\text{grain}}^{\text{max}}} = C \left(\frac{\mu^{\text{dg}}}{\tilde{\alpha}_m} \right), \end{aligned} \quad (5)$$

where n_{grain} is the number density of dust grains, $\tilde{\alpha}_m$ is the dimensionless maximum grain size parameter ($\tilde{\alpha}$ evaluated at $\epsilon_{\text{grain}} = \epsilon_{\text{grain}}^{\text{max}}$), and C is a constant of order 20.

Another useful parameter is the 'free streaming length' of the dust (relative to the gas),

$$\frac{\ell_{\text{stream, dust}}}{H_{\text{gas}}} \sim 10^{-4} \left(\frac{\epsilon_{\text{grain}}}{\mu\text{m}} \right) \left(\frac{10^{24} \text{ cm}^{-2}}{N_{\text{H, gas}}} \right) \propto \tau_{\text{geo}}^{-1}. \quad (6)$$

Therefore, for all our simulations, the grains are 'well coupled' to the gas in the sense that $\ell_{\text{stream, dust}} \ll H_{\text{gas}}$, so we do not expect them to simply 'eject' from the gas without interacting and sharing momentum.

3.1 Parameters and physics with weak effects

We now discuss physical parameters that we tested, but found to have weak to no effect on the behaviour of the instabilities within this regime including magnetic field strength, magnetic field direction, AGN luminosity, grain charge, and strength of gravity.

3.1.1 Charging physics and magnetic field strength

We ran tests varying the magnetic field strength B_0 , or equivalently the plasma β , and magnetic field orientation θ_B within the box. Similarly, as the grain charge is unconstrained, we consider different grain charging mechanisms (collisional versus photoelectric) and found these parameters to have a negligible effect on the long-term behaviour of the instabilities. This is due to two reasons. First, this arises naturally within AGN-like environments where Lorentz forces are weak relative to the drag force, i.e. $t_s/t_L \sim \tilde{\phi}_m/\tilde{\alpha}_d^{1/2} \ll 1$ where $\tilde{\phi} \equiv 3 Z_{\text{grain}}^0 [\epsilon_{\text{grain}}^{\text{max}}] e / (4\pi c (\epsilon_{\text{grain}}^{\text{max}})^2 \rho_{\text{base}}^{1/2})$ is the dimensionless grain charge parameter, and $\tilde{\alpha}_d \equiv (3/4) (F_0 \langle Q \rangle_{\text{ext}} / c) / (\rho_{\text{base}} c_s^2)$ is the dimensionless dust acceleration parameter. Secondly, the dominant modes in our simulations are in the 'long-wavelength regime', and hence, are only weakly sensitive to magnetic effects as the magnetic pressure and tension provide only second-order corrections to what is to leading order a 'collisionless' or 'pressure-free' mode (Hopkins & Squire 2018a). Therefore, we observe that at early stages of the RDIs' development, amplified magnetic fields, or higher grain charge-to-mass ratios merely result in density perturbations propagating at slightly different angles $\sim \theta_B$, but the fluid flow retains its general properties. Further, as the instabilities reach the non-linear stage of their evolution, this propagation angle decreases till the fluid is moving roughly parallel to the vertical acceleration, and we see essentially no effect on the medium.

3.1.2 Thermal state of gas

We find that the choice of the thermal equation of state of the gas γ , and therefore the speed of sound c_s do not affect our results. As the grains are accelerated to supersonic velocities, c_s factors out of the relevant equations such as the stopping time and the growth rates of the modes to leading order in the linear theory for these particular long-wavelength modes of interest.

3.1.3 Gravity

Further, as shown in Table A1, for this environment, the strength of gravity is much weaker than the acceleration due to radiation, i.e. $\tilde{g}/\tilde{\alpha}_d \sim 10^{-3} (\epsilon_{\text{grain}}^{\text{max}}/\mu\text{m})$, where $\tilde{g} \equiv |\mathbf{g}| H_{\text{gas}}/c_s^2$ is the dimensionless gravity parameter and $\tilde{\alpha}_d \equiv (3/4) (F_0 \langle Q \rangle_{\text{ext}} / c) / (\rho_{\text{base}} c_s^2)$ is the dimensionless acceleration parameter. Thus, gravity acts merely to ensure that the gas that is left behind the wind 'falls back', but does not have a noticeable effect on the general behaviour of the RDIs. It is easy to verify that for the conditions and time-scales we emulate here, the self-gravity of the gas should also be unimportant.

3.1.4 AGN luminosity

Naively, the AGN luminosity should have an important effect here. However, in the dimensionless units in which we will work, i.e. length in units of $\sim H_{\text{gas}} \sim r_{\text{sub}}$, time in units of the 'acceleration time' defined below, the absolute value of the AGN luminosity factors out completely. None the less, while the AGN luminosity does not affect the qualitative behaviour of the RDIs (in the appropriate units), it effectively defines the characteristic time and spatial scales of the problem. For example, the AGN luminosity normalizes the sublimation radius, i.e. $r_{\text{sub}} \sim 0.3 \text{ pc } L_{46}^{1/2}$. This means if we define the flux at the base of our box as the flux at r_{sub} (as we do), the AGN luminosity factors out [the flux at r_{sub} is, by definition, fixed (Ivezić & Elitzur 1997)], and we find that the vertical acceleration of the column, $a_{\text{eff}} \equiv \mu^{\text{dg}} a_{\text{dust}} - g \sim a_{\text{eff}} \equiv \mu^{\text{dg}} a_{\text{dust}}$, where a_{dust} is the acceleration experienced by the dust, has the following scaling:

$$a_{\text{eff}} \sim 0.3 \text{ cm s}^{-2} \left(\frac{1 \mu\text{m}}{\epsilon_{\text{grain}}^{\text{max}}} \right), \quad (7)$$

which is independent of the AGN luminosity, and only depends on the maximum size of the grains.

It is worth noting that our choice of normalization is not arbitrary. In the context of dust-driven winds, our focus is on regions where dust is present, i.e. beyond the sublimation radius. When the radius is much smaller than the sublimation radius ($r \ll r_{\text{sub}}$), the dust is expected to be sublimated, and the dominant mechanism for driving the wind would be line-driving rather than dust absorption (Proga, Stone & Kallman 2000). Conversely, when the radius is much larger than the sublimation radius ($r \gg r_{\text{sub}}$), the radiation flux decreases according to the inverse square law. In our simulations, we observe that the wind originates from the base of the column where the radiation flux is strongest, which aligns with our expectations. The sublimation radius can be derived analytically assuming thermal equilibrium, allowing us to express the sublimation radius as $r_{\text{sub}} \sim (L_{\text{QSO}}/4\pi\sigma_{\text{SB}}T_{\text{sub}}^4)^{1/2}$. Therefore, since the location of the dusty torus is proportional to $\sqrt{L_{\text{QSO}}}$, the flux at the inner edge of the torus is independent of luminosity. This size–luminosity relation has been supported by observational studies (Suganuma et al. 2006; Tristram et al. 2009b; Kishimoto et al. 2011b). However, it is important to note that the theoretical relation strongly depends on the

sublimation temperature, which in turn depends on grain composition which is uncertain. In our simulations, we assume a silicate grain composition corresponding to a sublimation temperature of 1500 K. Nevertheless, different grain compositions within the torus can result in sublimation temperatures ranging from ~ 1300 to 2000 K. This variation influences the flux and acceleration time-scales of the winds, resulting in a fractional variation of 0.6 for the sublimation radius, where smaller (larger) radii would correspond to shorter (longer) time-scales for wind launching.

However, the argument above assumes that the flux is stronger than the gravitational pull of the central source, allowing the initiation of a wind. Therefore, the luminosity does not affect the behaviour of the wind insofar as this condition is met.

The luminosity does however normalize the bulk acceleration time-scale which depends on both $H_{\text{gas}} \sim r_{\text{sub}}$ and a_{eff} , as

$$t_{\text{acc}} \equiv \sqrt{\frac{20H_{\text{gas}}}{a_{\text{eff}}}} \sim 245 \text{ yrs } L_{46}^{1/4} \left(\frac{\epsilon_{\text{grain}}^{\text{max}}}{\mu\text{m}} \right)^{1/2} \left(\frac{0.01}{\mu^{\text{dg}}} \right)^{1/2}, \quad (8)$$

corresponding to the time when a perfectly coupled dust + gas fluid would have reached a height $z \sim 10 H_{\text{gas}}$. As we normalize our parameters to the sublimation radius r_{sub} and the bulk acceleration time-scale t_{acc} , our findings are independent of the AGN luminosity. However, if the dust were held at a fixed radius while varying the luminosity, the flux at the sublimation radius would change, which could alter the dynamics of the fluid and thus, affect the behaviour of the RDIs.

3.2 Parameters with strong effects: the geometric optical depth

Our results are sensitive to the choice of grain size and column density, as they determine the critical wavelength and thus the dominant mode of the instability. Specifically, from equation (3), we can see the ratio of the largest scale mode with $\lambda \sim H_{\text{gas}}$ to critical wavelength can be expressed as

$$\frac{H_{\text{gas}}}{\lambda_{\text{crit}}} \sim \frac{H_{\text{gas}}}{\langle \mathbf{w}_s \rangle t_s / \mu^{\text{dg}}} \sim \frac{\mu^{\text{dg}} H_{\text{gas}}}{\bar{\rho}_{\text{grain}}^i} \left(\frac{\rho_g}{\epsilon_{\text{grain}}} \right) \sim \frac{\mu^{\text{dg}}}{\tilde{\alpha}_m} = \frac{\tau_{\text{geo}}}{C} \sim 300 \left(\frac{\mu^{\text{dg}}}{0.01} \right) \left(\frac{N_{\text{H}}}{10^{24} \text{ cm}^{-2}} \right) \left(\frac{1 \mu\text{m}}{\epsilon_{\text{grain}}^{\text{max}}} \right), \quad (9)$$

where $C \sim 20$ is a constant defined earlier.

Again, as $H_{\text{gas}}/\lambda_{\text{crit}} \gg 1$ for the typical values of $(\rho_g/\epsilon_{\text{grain}}^{\text{max}})$, the dominant modes are always in the long-wavelength regime. Additionally, we note the regime of the instabilities strictly depends on the geometrical optical depth, where an environment with $\tau_{\text{geo}} \gtrsim 20$ would be sufficient to satisfy the criteria for the ‘long-wavelength RDI’ regime.

Further, we can compare the instability growth time to the wind’s acceleration time. As $a_{\text{eff}} \gg c_s/t_s^0$, where t_s^0 is the stopping time at $t = 0$, we assume that the dust is drifting supersonically and use the expression for the equilibrium drift velocity in the supersonic limit derived in Hopkins & Squire (2018b) (i.e. $\langle \mathbf{w}_s \rangle \sim \sqrt{a_{\text{dust}} t_s^0 c_s}$) with direction $\hat{\mathbf{w}}_s$ to obtain

$$\frac{t_{\text{acc}}}{t_{\text{grow}}} = \left(\frac{20H_{\text{gas}}}{a_{\text{dust}}} \right)^{1/2} \left(\frac{(\mathbf{k} \cdot \mathbf{w}_s)^4}{\mu^{\text{dg}} \langle t_s \rangle^2} \right)^{1/6} \sim 4.7 (H_{\text{gas}} \mathbf{k} \cdot \hat{\mathbf{w}}_s)^{2/3} \left(\frac{\tilde{\alpha}}{\mu^{\text{dg}}} \right)^{1/6} \propto \tau_{\text{geo}}^{-1/6}. \quad (10)$$

Note that $H_{\text{gas}} \mathbf{k} \cdot \hat{\mathbf{w}}_s \sim 1$ and that $\mu^{\text{dg}}/\tilde{\alpha}_m \sim \tau_{\text{geo}}/C$. Hence, the characteristic time-scales and length-scales only depend on τ_{geo} or the ratio $\mu^{\text{dg}} N_{\text{H}}/\epsilon_{\text{grain}}^{\text{max}}$, yielding similar behaviours for similar ratios. As $t_{\text{acc}}/t_{\text{grow}} \propto \tau_{\text{geo}}^{-1/6}$, lower τ_{geo} (lower column density and larger grains) imply shorter growth times, i.e. more e-folding times for the clumping to amplify. This would result in filaments with stronger clumping and higher variability. However, we note that this trend is weak $\sim \tau_{\text{geo}}^{1/6}$, so we observe similar levels of clumping/variability across the parameter space we explore.

From the relations obtained in equations (9) and 10, it is evident that μ^{dg} plays a crucial role in shaping the spatial and temporal behaviour of the RDIs. In our simulations, we have employed a fixed value of $\mu^{\text{dg}} = 0.01$. However, it is important to recognize that this parameter will vary depending on the AGN environment and metallicity Z . The connection between μ^{dg} and Z is derived based on the assumption that dust formation and destruction time-scales exhibit similar dependencies on time (Dwek 1998). To first-order, this leads to a constant dust-to-metal mass ratio and a dust-to-gas ratio that scales with metallicity as $\mu^{\text{dg}} \propto Z$, which is supported by observational studies (e.g. James et al. 2002; Draine et al. 2007; Bendo et al. 2010; Magrini et al. 2011). For $\mu^{\text{dg}} \gg 0.01$, we anticipate minimal deviations in RDI behaviour, as the RDIs would still reside within the long-wavelength regime. Although the ratio $t_{\text{acc}}/t_{\text{grow}}$ would be reduced according to $t_{\text{acc}}/t_{\text{grow}} \propto (\mu^{\text{dg}})^{-1/6}$, the impact is not substantial. However, increasing μ^{dg} would result in a higher dust opacity, thereby requiring a lower UV luminosity to initiate outflows. In addition, these outflows would have shorter acceleration times ($t_{\text{acc}} \propto (\mu^{\text{dg}})^{-1/2}$). In environments where $\mu^{\text{dg}} \ll 0.01$, a shift in RDI behaviour may occur. Specifically, in low-density columns ($N_{\text{H}} \leq 10^{22} \text{ cm}^{-2}$) with maximum grain sizes $\epsilon_{\text{grain}}^{\text{max}} \geq 1 \mu\text{m}$, the RDIs could transition to the mid-wavelength regime due to the linear dependence of $H_{\text{gas}}/\lambda_{\text{crit}}$ on μ^{dg} .

However, in order to induce significant changes in RDI behaviour driven by variations in metallicity or the dust-to-gas ratio, μ^{dg} would need to undergo a shift of at least one order of magnitude. Observations suggest that the majority of AGN environments exhibit solar-to-supersolar metallicities (Storchi-Bergmann et al. 1998; Hamann et al. 2002). Low-metallicity AGN sources have been observed; however, they only display marginal deviations below solar metallicity (Groves, Heckman & Kauffmann 2006; Polimera et al. 2022; Übler et al. 2023).

4 RESULTS

4.1 General profile of the outflow and large-scale morphology

To understand how the RDIs affect the dynamics of the dusty torus, we first consider the resulting morphology within a relatively small patch within the torus. However, as we are not modelling the entire region around the AGNs, we cannot draw definitive conclusions about how the RDIs affect the overall morphology of the AGN torus or its geometry. The results we present in Fig. 2 show the temporal evolution of the gas (left) and the dust (right) column densities for a run with $N_{\text{H}} \sim 10^{24} \text{ cm}^{-2}$ and $\epsilon_{\text{grain}} \sim 1 \mu\text{m}$ in the xz plane within $z \sim 0 - 9 H_{\text{gas}}$ at $t \sim (0, 0.3, 0.5) t_{\text{acc}}$. These plots illustrate the successful launch of a radiation-driven wind with strong gas-dust coupling and the formation of elongated filaments on large scales. At $t \sim 0$, the fluid is vertically stratified as per our initial conditions. The RDIs have growth times that are short relative to the flow time, with the largest scale modes growing at a fraction ($\sim 10^{-1}$) of wind acceleration time. While the instabilities are within the linear regime,

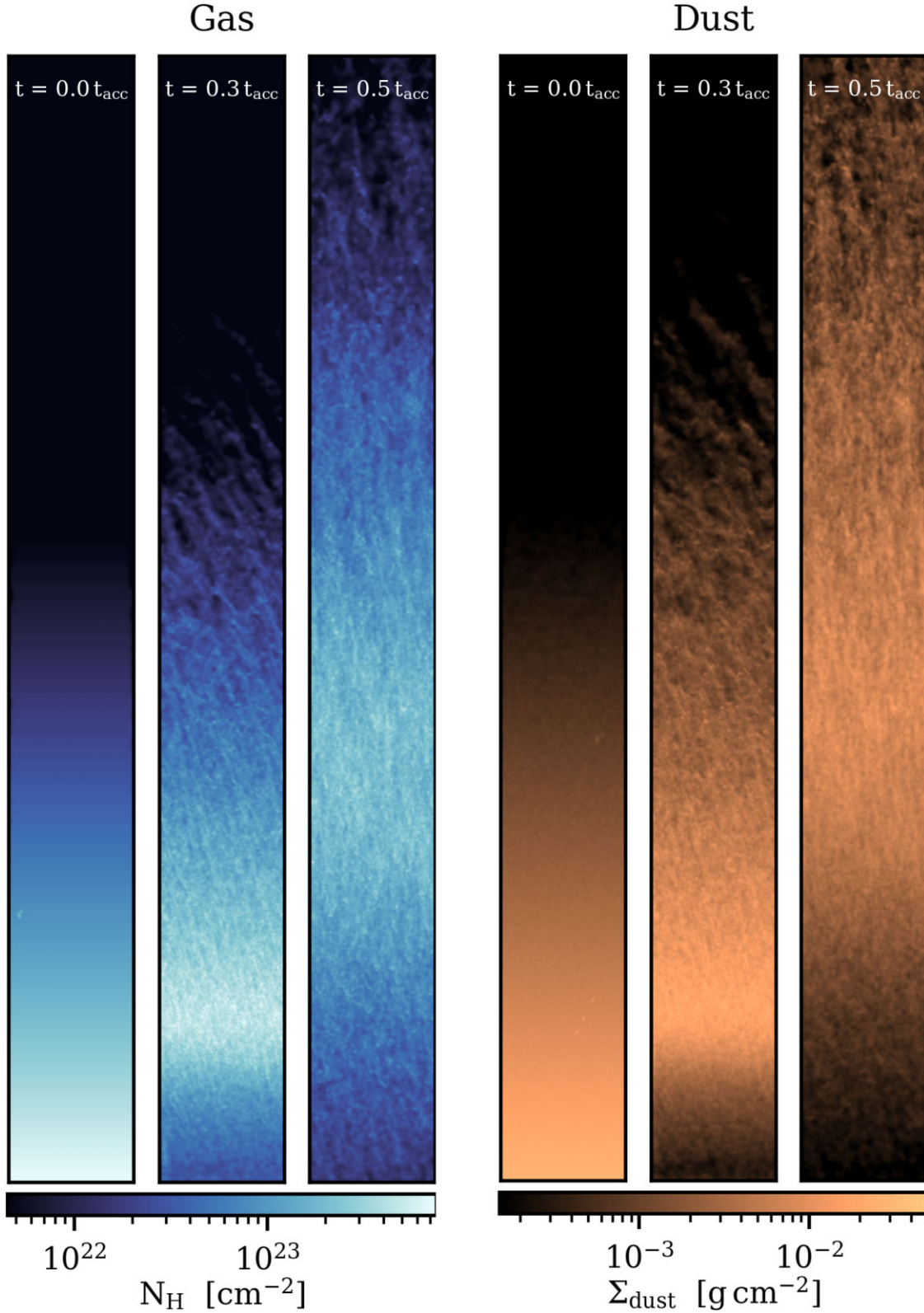


Figure 2. The evolution of the gas (left), and dust (right) column density for a simulation box with $N_{\text{H}} \sim 10^{24} \text{cm}^{-2}$ and $\epsilon_{\text{grain}}^{\text{max}} \sim 1 \mu\text{m}$ in the xz plane within $z \sim 0-9 H_{\text{gas}}$ at $t \sim (0.0, 0.3, 0.5) t_{\text{acc}}$, where t_{acc} corresponds to the acceleration time-scale defined as $t_{\text{acc}} \equiv (20 H_{\text{gas}} / \langle a_{\text{eff}} \rangle)^{1/2}$ with $\langle a_{\text{eff}} \rangle \equiv \langle \mu^{\text{dg}} a_{\text{dust, rad}} \rangle - g$, when a perfectly coupled fluid would have reached a height $z \sim 10 H_{\text{gas}}$. All simulations within our set show winds that were successfully launched with high degrees of clumping on small spatial scales and vertical filaments on large scales. The RDIs develop within a fraction of wind acceleration time ($t_{\text{grow}} \sim 10^{-1} t_{\text{acc}}$) with similar structures for the gas and dust. The filaments that form are initially inclined with respect to the \hat{z} direction and align along the \hat{z} -axis at later times ($t \sim 0.5 t_{\text{acc}}$).

the gas and negatively charged dust develop density perturbations in the form of sinusoidal waves at an inclination angle $\sim -\theta_B^0$ from the vertical axis. As the instabilities evolve non-linearly, the inclined filaments begin aligning with the vertical axis forming elongated structures that continue to accelerate upwards.

The centre of the wind, which we define as the region containing a dominant fraction of the dust (60 per cent by mass of the dust within the central region with 20 per cent below and above the region), reaches a height similar to that expected for a perfectly coupled homogeneous fluid without any RDIs present. However, we find that only ~ 50 per cent of the gas remains within such heights, with roughly 40 per cent of the gas ‘lagging’ behind the wind. This suggests that while there exists strong micro-scale coupling between the dust and the gas through drag forces, the overall fluid is not perfectly coupled resulting in a significant fraction of the dust ‘leading’ in front of the gas.

Additionally, we find that the cumulative mass fraction (CMF) profile of the outflow strongly depends on the parameters we explore within our simulation set. As depicted in Fig. 3, we present the CMF profile of the gas and dust at $t \sim t_{\text{acc}}$ for different simulations. To demonstrate the effects of varying column densities, the top panel shows the results for simulations with maximum grain size $\epsilon_{\text{grain}}^{\text{max}} \sim 0.1 \mu\text{m}$, and average column density $N_{\text{H}} \sim 10^{22} \text{cm}^{-2}$, $N_{\text{H}} \sim 10^{24} \text{cm}^{-2}$, and $N_{\text{H}} \sim 10^{26} \text{cm}^{-2}$. Meanwhile, to show the grain size dependence, the bottom panel displays the CMF profile for simulations with an average column density of $N_{\text{H}} \sim 10^{24} \text{cm}^{-2}$ and maximum grain sizes of $\epsilon_{\text{grain}}^{\text{max}} \sim 0.01 \mu\text{m}$, $\epsilon_{\text{grain}}^{\text{max}} \sim 0.1 \mu\text{m}$, and $\epsilon_{\text{grain}}^{\text{max}} \sim 1 \mu\text{m}$. Although the gas and dust have similar CMF profiles, the fluid is not perfectly coupled, with the gas ‘lagging’ behind the dust. This lagging effect increases with increasing grain size and decreasing density as predicted in equation (6). In our runs with higher column densities ($N_{\text{H}} \sim 10^{25} - 10^{26} \text{cm}^{-2}$), the two plots roughly overlap as the fluid becomes closer to a perfectly coupled fluid on large scales. To measure the impact of imperfect coupling between gas and dust, we analyse the CMFs of the gas compared to the dust at $t = t_{\text{acc}}$. By comparing the height range that encompasses 25–75 per cent of the dust to the corresponding gas mass within that range, we can quantify this effect. Our findings show that, on average, the dusty gas can successfully eject around 70–90 per cent of the gas present. This implies that the torus is not a static or constant structure, but rather subject to substantial variations over time. If a high-luminosity state persists for a sufficient duration to drive a wind, it is anticipated that the torus would disappear. This aligns with the receding torus framework as proposed in Lawrence (1991), Simpson (2005), and Hoenig & Beckert (2007).

4.2 Effects of full RDMHD

In Figs 2 and 4, we compare the morphology of the simulations for our full RDMHD runs² (Fig. 4) versus the approximate ‘homogeneous flux’ ($F_0 = \text{constant}$) simulations (Fig. 2). Our RDMHD simulations employ a grey band approach with a photon injection rate of $\sim L/c$ where the optical depth (τ_{IR}) is set to crudely represent the IR opacity

²In these simulations, we can optionally employ a reduced speed of light (RSOL) (see Hopkins et al. 2022), $\tilde{c} < c$. In tests, we find identical results for $\tilde{c} \sim (0.1-1)c$ at $N_{\text{H}} \lesssim 10^{25} \text{cm}^{-2}$, so we use $\tilde{c} = 0.1c$ here so we can run at our higher fiducial resolution. For $N_{\text{H}} \gtrsim 10^{25} \text{cm}^{-2}$, however, finite speed of light effects are important so we use $\tilde{c} = c$ (no RSOL). This imposes a large CPU cost (shorter time-steps), so the full RDMHD simulations of $N_{\text{H}} \gtrsim 10^{25} \text{cm}^{-2}$ use 10x fewer resolution elements.

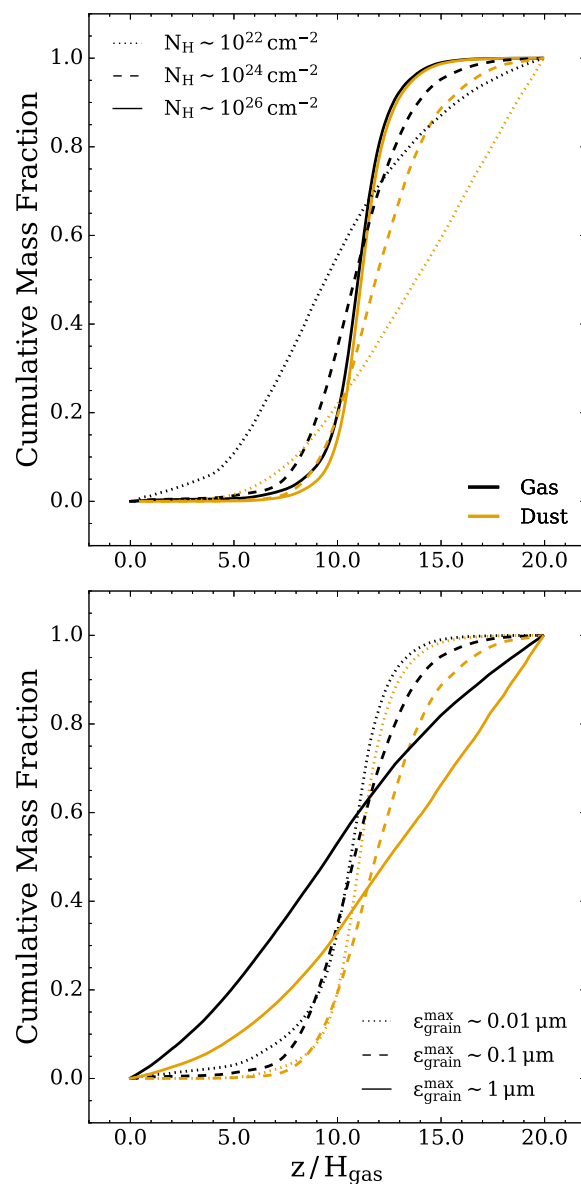


Figure 3. CMF profile of the gas (black) and the dust (yellow) for different column densities and maximum grain sizes. The top panel displays the results for a fixed maximum grain size of $\epsilon_{\text{grain}}^{\text{max}} \sim 0.1 \mu\text{m}$ and column densities of $N_{\text{H}} \sim 10^{22} \text{cm}^{-2}$ (dotted line), $N_{\text{H}} \sim 10^{24} \text{cm}^{-2}$ (dashed line), and $N_{\text{H}} \sim 10^{26} \text{cm}^{-2}$ (solid line) at $t \sim t_{\text{acc}}$. The bottom panel shows the profiles for a fixed column density of $N_{\text{H}} \sim 10^{24} \text{cm}^{-2}$ and different maximum grain sizes: $\epsilon_{\text{grain}}^{\text{max}} \sim 0.01 \mu\text{m}$ (dotted line), $\epsilon_{\text{grain}}^{\text{max}} \sim 0.1 \mu\text{m}$ (dashed line), and $\epsilon_{\text{grain}}^{\text{max}} \sim 1 \mu\text{m}$ (solid line). At high column densities and small grain sizes, the gas and dust show similar profiles, but the fluid is not perfectly coupled, with the gas ‘lagging’ behind the dust. This decoupling becomes more pronounced at lower column densities and larger grain sizes as $\ell_{\text{stream, dust}} \propto \ell_{\text{grain}} N_{\text{H}}^{-1}$.

of the column. Therefore, the values we present for τ_{IR} should serve as rough estimates rather than precise values as we do not account for effects like the wavelength dependence of the opacity or photon degradation. From left to right in Fig. 4, the simulations correspond to columns with $N_{\text{H}} \sim 10^{22} \text{cm}^{-2}$, 10^{24}cm^{-2} , 10^{26}cm^{-2} , respectively, and $\epsilon_{\text{grain}}^{\text{max}} \sim 1 \mu\text{m}$ at $t \sim 0.5 t_{\text{acc}}$. We discuss the different regimes shown in this figure in the subsections below.

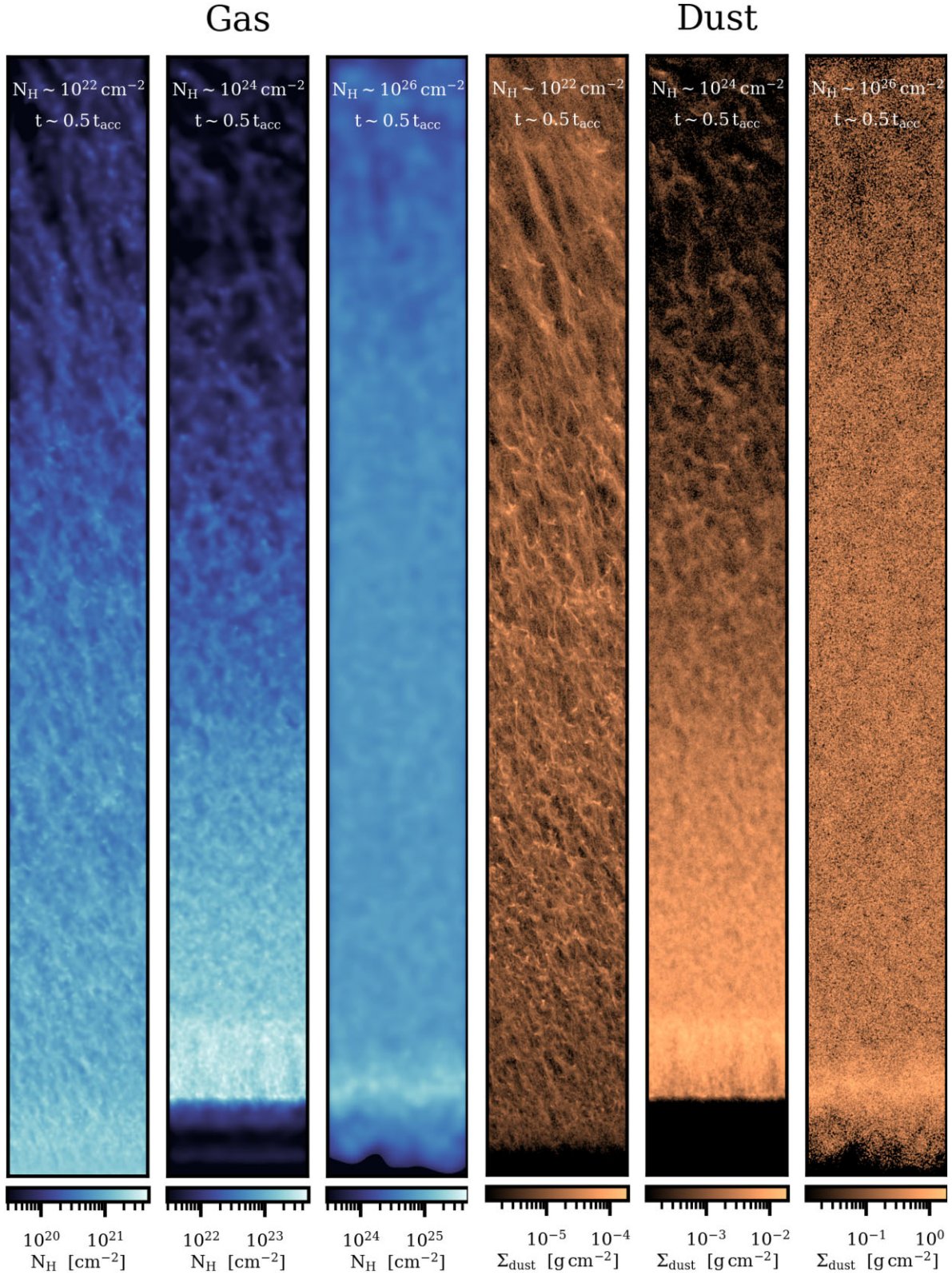


Figure 4. The gas (left) and dust (right) column densities for full RDMHD runs projected on the xz plane within $z \sim 1-9 H_{\text{gas}}$ at $t \sim 0.5 t_{\text{acc}}$. From left to right, the simulations correspond to runs with $\epsilon_{\text{grain}}^{\text{max}} \sim 1 \mu\text{m}$, and $\bar{c} \sim (0.1, 0.1, 1) c$, $N_{\text{H}} \sim 10^{22} \text{ cm}^{-2}$, 10^{24} cm^{-2} , 10^{26} cm^{-2} corresponding to $\tau_{\text{geo}} \sim 20, 2000, 2 \times 10^5$ ($\tau_{\text{IR}} \sim 0.2, 20, 2000$), respectively. Note that the rightmost plot shows less small-scale structure due to a factor of 10 reduction in resolution (owing to the cost of using $\bar{c} = c$). For the $N_{\text{H}} \sim 10^{22} \text{ cm}^{-2}$ and 10^{24} cm^{-2} , the optical depth is sufficiently low such that full treatment of RDMHD shows similar structure formation on small and large scales to the runs without explicit radiative transfer. For the $N_{\text{H}} \sim 10^{26} \text{ cm}^{-2}$ column, the high optical depth results in photon diffusion time that are longer than the wind acceleration time expected from a constant flux assumption resulting in a slower outflow.

4.2.1 Intermediate optical depths and the ‘acceleration-limited’ regime

For this regime, we consider the left and middle panels in Fig. 4 with $N_H \sim 10^{22} \text{ cm}^{-2}$ and $N_H \sim 10^{24} \text{ cm}^{-2}$, which correspond to $\tau_{\text{geo}} \sim 20$ ($\tau_{\text{IR}} \sim 0.2$) and $\tau_{\text{geo}} \sim 2000$ ($\tau_{\text{IR}} \sim 20$), respectively. With reference to Fig. 2, we can see that to first order, the large-scale morphology of the RDIs does not show any significant changes when the simulations are run with our full radiative transfer treatment versus simply assuming a homogeneous radiation field. We do note the formation of a thin high-density ‘slab’ at the base of the box in the middle panel of Fig. 4. This ‘slab’ acts as an opaque wall that gets lifted by the incident photons, and effectively translates the wind upwards without significant distortions to its morphology. None the less, this ‘slab’ does not significantly affect the integrated surface density along the line of sight or any of the macro-scale properties of the column above it, such as the CMF or clumping factor profile. Therefore, we conclude that using the homogeneous radiation approximation is sufficient within this regime. We emphasize, as shown in the following section, that the key factor is the radiation diffusion time compared to the wind launch and instability growth time-scales. When the radiation diffusion time is fast compared to these time-scales, the radiation field is smooth, and the homogeneous radiation approximation is valid.

4.2.2 Extremely large optical depths: the radiation-propagation-limited regime

For this regime, we consider the panel on the right in Fig. 4 with $N_H \sim 10^{26} \text{ cm}^{-2}$, which corresponds to $\tau_{\text{geo}} \sim 2 \times 10^5$ ($\tau_{\text{IR}} \sim 2000$). We point out that the plot displays less small-scale structure than the panels on the left due to the reduced resolution of the simulation (as noted above, this owes to using no ‘reduced speed of light’ here, which imposes a steep computational cost penalty). For this case, when accounting for full radiative transfer, the fluid is found to be accelerated to a lower height than expected. This result can be attributed to the breakdown of the assumption of an infinitesimally small photon diffusion time-scale (constant flux field). As the photons travel through the fluid, they ‘lag’ behind the wind due to propagation effects, leading to a decrease in the radiative acceleration and consequently, the fluid being accelerated to a lower height than expected. To determine when this occurs, we consider the ratio of the photon diffusion time, t_{diff} , to the dust acceleration time. For simplicity, we ignore the effects of gravity and assume a homogeneous dust–gas distribution. Therefore, the ratio of the time needed for a photon to diffuse through a distance H_ν (the ‘width’ of the gas ‘shell’) to the time required to accelerate the same ‘shell’ to a height of $10 H_{\text{gas}}$ has the following scaling:

$$\begin{aligned} \frac{t_{\text{diff}}}{t_{\text{acc}}} &= \frac{H_\nu^2 \mu^{\text{dg}} \rho_g \kappa a_{\text{eff}}^{1/2}}{\sqrt{20 H_{\text{gas}} c}} \\ &= \frac{3}{8\sqrt{5}} \frac{c_s}{c} (Q_{\text{ext}}) \bar{a}_d^{1/2} \left(\frac{\mu^{\text{dg}}}{\bar{a}_m} \right)^{3/2} \left(\frac{H_\nu}{H_{\text{gas}}} \right)^2 \\ &\sim 5 \times 10^4 \left(\frac{c_s/c}{10^{-5}} \right) \left(\frac{Q_{\text{ext}}}{1} \right) \left(\frac{\bar{a}_d}{5 \times 10^7} \right)^{1/2} \left(\frac{\tau_{\text{geo}}}{2 \times 10^4} \right)^{3/2} \left(\frac{H_\nu}{H_{\text{gas}}} \right)^2, \end{aligned} \quad (11)$$

where κ is the dust opacity, and we assume that $c_s/c \sim 10^{-5}$ ($T_{\text{gas}} \sim 1000 \text{ K}$), matching the assumptions used in our simulations. For simplicity, we assume that the grains all have the median grain size ($\epsilon_{\text{grain}} \sim 0.1 \epsilon_{\text{grain}}^{\text{max}}$) and not a grain size spectrum. It is important to note that the expression above is sensitive to the value of τ_{geo} . When comparing our lowest optical depth simulation ($N_H \sim 10^{22} \text{ cm}^{-2}$) to our highest ($N_H \sim 10^{26} \text{ cm}^{-2}$), there is an increase of a factor of 10^4 in τ_{geo} , which in turn results in a factor of 10^6 in the ratio of the

two time-scales considered above. Therefore, in the higher optical depth case, the radiation can no longer propagate fast enough to reach the material at the top of the box to maintain a constant flux. Consequently, material at the ‘top’ of the box in the ICs can fall down before radiation reaches it and the outflow propagation speed is limited not just by naive total acceleration but also photon transport time, resulting in a wind with a slower outflow velocity. However, despite the morphological change on large scales, this effect mostly acts to reduce the vertical translation of material in the column at a given time and has minimal effect on the internal properties of the outflow.

4.3 Do winds launch?

As shown in Figs 2 and 3, our plots indicate that the accelerated dust imparts sufficient momentum on to the gas to successfully launch a wind across our entire parameter survey. As photons propagate through the box, they could in principle escape through low-density ‘channels’, and thus, impart lower amounts of their momentum on to the dust resulting in $p^{\text{total}} < p^{\text{MS}} \equiv \int \tau_{\text{IR}} L/c dt$, where p^{total} and p^{MS} denote the total momentum carried by the fluid and the expected momentum for the multiple scattering regime, respectively. We show the gas and dust components of the total momentum (note that we multiply the dust momentum by a factor of $1/\mu^{\text{dg}} = 100$ for ease of comparison) in the wind relative to the predicted momentum p^{MS} in Fig. 5. The plots show that prior to the growth time for the instabilities, $t \lesssim 0.1 t_{\text{acc}}$, the radiation is well coupled to the fluid. However, as the instabilities grow, the line for the expected momentum begins to separate from the imparted momentum as low-density ‘channels’ develop. When the total momentum of the fluid in the simulation is lower than the expected value, we define this as momentum ‘leakage’. This situation indicates a lack of efficient momentum transfer between the injected radiation and the dusty fluid. At $t \sim t_{\text{acc}}$, the plots show factors 1–3 of momentum ‘leakage’ from the box which increases with increasing column density. We attribute this effect to slower photon diffusion at higher column densities which results in an overall reduced incident flux on the dust particles. But we still always see an order-unity fraction of the radiation momentum p^{MS} actually couples, and thus is always sufficient to launch a wind under AGN-like conditions as simulated here.

We compare our simulations to the simulations conducted by Venanzi et al. (2020) and Arakawa et al. (2022) modelling AGN winds driven by radiation pressure on dust. A key distinction in our approach is that we explicitly account for dust dynamics, which was not taken into consideration in the previous simulations. Consistent with the findings of Arakawa et al. (2022), we observe that the acceleration of the gas column remains unaffected by column density in the multiple scattering regime ($N_H \sim 10^{22}–10^{24} \text{ cm}^{-2}$), as indicated by equation (8). Additionally, we also demonstrate that increasing the grain size leads to weaker acceleration due to the reduction in dust absorption cross-section. In contrast, within the highly optically thick regime ($N_H \sim 10^{26} \text{ cm}^{-2}$), denser gas columns experience a lower effective acceleration due to the absorption of UV flux by a thin inner shell, resulting in reduced momentum transfer from the outer shell. These findings align with the previous studies mentioned. To further support our observations, we calculate the $t_{\text{diff}}/t_{\text{acc}}$ ratio in equation (11), which further validates the conclusions. However, it is important to acknowledge that our simulations may underestimate this effect since we did not account for photon downgrading, which has the potential to diminish the effectiveness of momentum transfer. Further, we find that the conditions in our simulations, which all result in successful

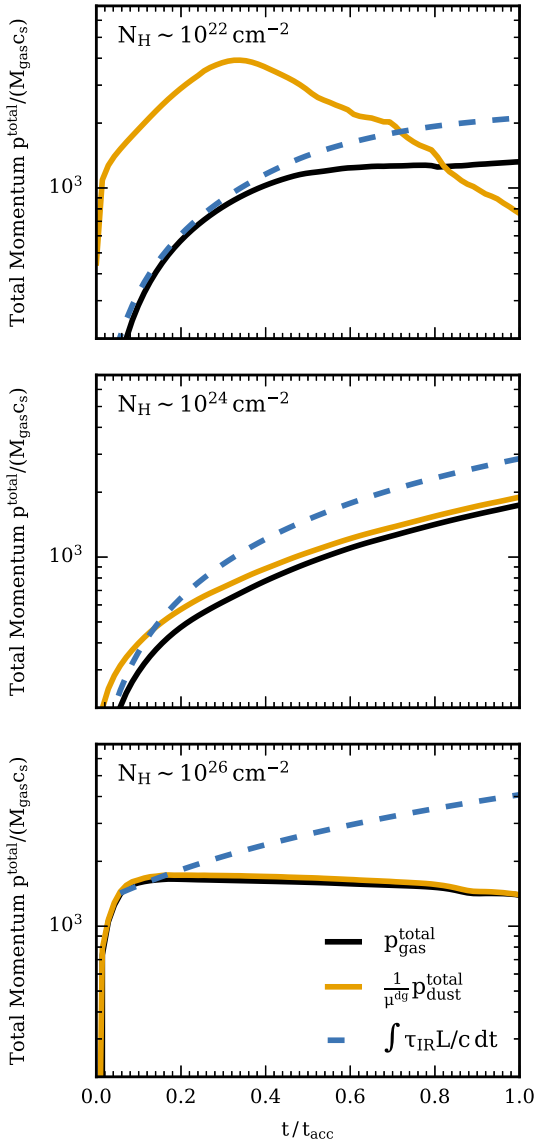


Figure 5. Gas (black) and dust (yellow) total momentum normalized to the product of the total gas mass within the box at $t = 0$ and the speed of sound compared to expected momentum in the wind (blue dotted line) in the homogeneous perfect-coupling grey opacity limit, $p^{\text{total}} \sim \int \tau_{\text{IR}} L/c dt$ for three RDMHD runs. Note that we multiply the dust momentum by a factor of $1/\mu^{\text{dg}} = 100$ for plotting purposes. From top to bottom, the total gas column density N_{gas} corresponds to 10^{22} , 10^{24} , and 10^{26} cm^{-2} , respectively, and maximum grain size of $1 \mu\text{m}$. The plots show factors of 1–3 momentum ‘leakage’, with higher leakage for denser columns. The top panel shows a turnover in the dust momentum as most energetic dust particles escape from the box.

outflows, also satisfy the outflow launching conditions outlined in the studies above.

However, the conditions required for torus ejection may not apply to all AGNs, and our simulation represents only one particular scenario. Our results are specific to the assumptions of a massive BH emitting at the Eddington limit, resulting in a high luminosity that ensures the ejection of dusty gas. This choice is made to ensure that the radiative acceleration is greater than the opposing gravity force and thus would result in the ejection of the dusty gas. As this condition would be maintained at larger distances from the AGN, if the AGN torus is successfully ejected, we expect it to escape the

gravitational pull of the BH. Therefore, it is plausible that the outflow from the torus is part of an evolutionary sequence as suggested by observations (Banerji et al. 2012; Glikman et al. 2012). However, our current simulations only focus on a small region, therefore, we cannot provide a comprehensive analysis on this topic at this stage.

We also study the behaviour of the wind in an environment where gravity dominates over the radiation-driven acceleration, i.e. where $\tau_{\text{IR}} L/c \lesssim g M_{\text{gas}}$, or in our dimensionless units $\tilde{\alpha}/\tilde{g} \lesssim 1$ (though we note we are only modestly in this regime here, with gravity a factor of ~ 3 stronger than radiation). We show the projected morphology of the gas column under these conditions evolved to $t \sim (0.4, 1.0, 1.3, 1.7) t_{\text{acc}}$ in Fig. 6. As the net vertical acceleration is in the negative \hat{z} direction, we define the acceleration time as $t_{\text{acc}} = \sqrt{20 H_{\text{gas}}/|a_{\text{eff}}|}$ for this simulation. The simulation is run with full RDMHD with the following parameters: $\tilde{c} \sim 0.1 c$, $N_{\text{H}} \sim 10^{24} \text{ cm}^{-2}$, and $\epsilon_{\text{grain}}^{\text{max}} \sim 0.01 \mu\text{m}$. Naively, we would expect a failed wind to result from these conditions; however, as shown in the plots, much of the gas (and dust as they are tightly coupled in this simulation) is successfully ejected. The increased strength of gravity does not cause the wind to halt, but rather compresses the gas and dust to a more compact ‘shell’. After the ejecta is compressed into a thin slab, the radiation continues to accelerate the material, resulting in a thicker slab with prominent substructure at later times. Some gas indeed ‘falls back’ – more than in our fiducial simulations with $\tilde{g} < \tilde{\alpha}$; but the same inhomogeneity that allows tens of per cent of gas to ‘fall down’ in those simulations leads to tens of per cent gas ejected here.

When comparing the wind energetics from our simulations with the observations of AGN galactic outflows, such as those reported in Fluetsch et al. (2018), we find relatively consistent values of ~ 50 per cent momentum loading within the wind relative to $\tau_{\text{IR}} L/c$. For our fiducial AGN luminosity of $10^{46} \text{ erg s}^{-1}$, this translates to momentum rates in the range of $10^{35} - 10^{37} \text{ g m s}^{-2}$ and kinetic rates in the range of $10^{43} - 10^{45} \text{ erg s}^{-1}$. However, we must emphasize that our simulations are highly idealized and are based on several assumptions about the set-up and thermodynamics of the outflow. For instance, our simulations do not account for the multiphase structure of the gas or the processes that may alter energy dissipation, such as heating and cooling due to photoelectric and radiative processes such as line emission.

Additionally, the existence of polar dusty outflows in AGNs has been suggested by recent interferometric observations (Asmus, Hoenig & Gandhi 2016; Hönig & Kishimoto 2017; Alonso-Herrero et al. 2021). However, it is important to note that this study is limited to a localized region within the obscuring torus, and that our simulations are agnostic to the overall geometry of the system. We explore different lines of sight and angles relative to the torus by varying the column density in our simulations. Specifically, the densest column density ($N_{\text{H}} \sim 10^{26} \text{ cm}^{-2}$) corresponds to roughly equatorial lines of sight, while a column density of $N_{\text{H}} \sim 10^{22} \text{ cm}^{-2}$ represents weakly obscured or more polar sight-lines. In Fig. 5, we demonstrate that at $N_{\text{H}} \sim 10^{22} \text{ cm}^{-2}$, our simulations still exhibit outflows. However, we would like to emphasize that this is expected because the simulations are set up such that radiation pressure on dust is stronger than the gravitational pull of the central source. It is important to acknowledge that our simulations treat all the physics consistently and assume the same dust composition throughout, without explicitly considering the properties of polar dust which could vary in composition and grain size (see Hönig & Kishimoto 2017; García-Bernete et al. 2022; Isbell et al. 2022). Regrettably, these factors are beyond the scope of this study. However, we recognize the significance of investigating these additional factors, and in future work, we intend to conduct more comprehensive

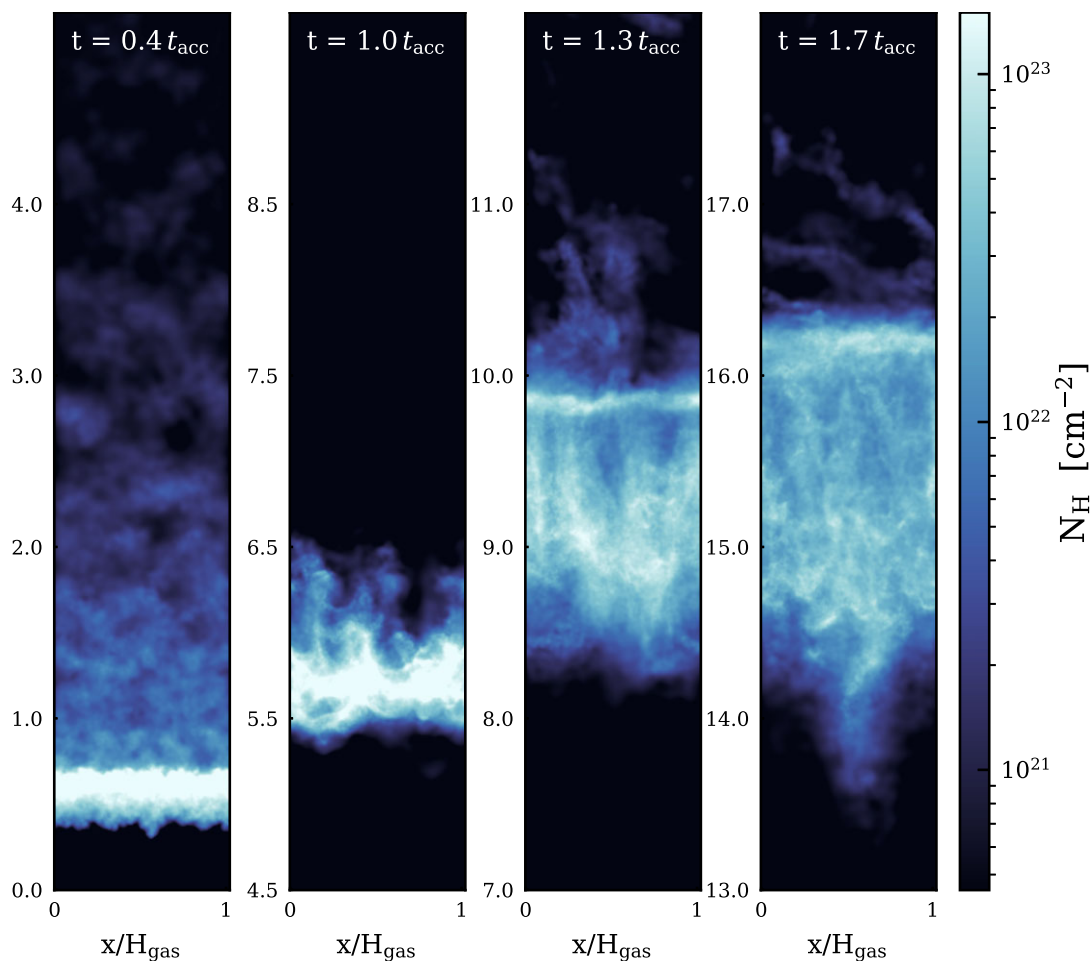


Figure 6. The evolution of the gas column density for an RDMHD simulation box with $\tilde{c} \sim 0.1c$, $N_{\text{H}} \sim 10^{24} \text{cm}^{-2}$, and $\epsilon_{\text{grain}}^{\text{max}} \sim 0.01 \mu\text{m}$ in the xz plane at $t \sim (0.4, 1.0, 1.3, 1.7) t_{\text{acc}}$, where for this case $t_{\text{acc}} = \sqrt{20H_{\text{gas}}/|a_{\text{eff}}|}$. For this simulation, we initialize the box such that in the perfect dust-to-gas coupling limit, the net force from gravity is stronger than the radiation pressure force by a factor of ~ 3 . The plot shows that despite the strength of gravity being stronger than the radiation-driven acceleration, a non-negligible component of the dust and gas is still ejected; however, the resulting ejecta is more compressed relative to our default set-up, and a somewhat larger fraction ‘falls back’.

simulations that encompass the entire region surrounding AGNs and account for the different dust properties.

4.4 Gas and dust clumping and coupling in AGN winds

As discussed above, we find that the dust and gas within the fluid are not always perfectly coupled. In Fig. 7, we quantify this by computing the gas–gas, dust–dust, and dust–gas clumping factors defined in equation (12), as a function of height within the simulation box at $t \sim \min(t_{\text{acc}}, t_{\text{esc}})$, where t_{esc} is the time at which 10 percent of the dust/gas has escaped the top of the box.

$$C_{nm} \equiv \frac{\langle \rho_n \rho_m \rangle_V}{\langle \rho_n \rangle_V \langle \rho_m \rangle_V} = \frac{V \int_V \rho_n(\mathbf{x}) \rho_m(\mathbf{x}) d^3\mathbf{x}}{\left[\int_V \rho_n(\mathbf{x}) d^3\mathbf{x} \right] \left[\int_V \rho_m(\mathbf{x}) d^3\mathbf{x} \right]} = \frac{\langle \rho_n \rangle_{M_m}}{\langle \rho_n \rangle_V} \quad (12)$$

As shown in the equation, the clumping factor is analogous to the autocorrelation (for like species) and the cross-correlation (for different species) function of the local density field, where factors less than 1 imply an anticorrelation. We report clumping factors ~ 1 – 10 for the gas–gas and dust–dust clumping factors, and ~ 1 for dust–gas clumping. The gas–gas clumping factors, C_{gg} , are lower

at the base of the wind and increase up to a roughly constant value within the accelerated wind. As the gas is collisional and pressurized, its clumping is limited by pressure forces, especially on small spatial scales inside the wind. We note that for the run with $N_{\text{H}} \sim 10^{22} \text{cm}^{-2}$, $\epsilon_{\text{grain}}^{\text{max}} \sim 1 \mu\text{m}$, the gas has high clumping factors at $z \sim 10 \rightarrow 20 H_{\text{gas}}$. This occurs for this parameter space, due to the low gas column density and high acceleration forces, which make the gas effectively more compressible. Within this environment, the gas is subjected to intense radiation, resulting in strong acceleration forces acting upon it. Low-density gas, characterized by higher compressibility, would experience larger relative fluctuations in density. These fluctuations give rise to localized density variations that exhibit strong correlations on small scales. As a consequence, the spatial density autocorrelation function reflects stronger correlations and higher clustering factors.

The dust–dust clumping factors, C_{dd} , show a constant rise as a function of height to reach maximal values at the top of the box, and the slope of the profile weakly increases with grain size and weakly decreases with density. However, the run with $N_{\text{H}} \sim 10^{22} \text{cm}^{-2}$, $\epsilon_{\text{grain}}^{\text{max}} \sim 1 \mu\text{m}$ shows a seemingly different behaviour as it corresponds to $t \sim t_{\text{esc}}$. In this case, t_{esc} is smaller than t_{acc} due to poor fluid coupling under the specific conditions of the simulation.

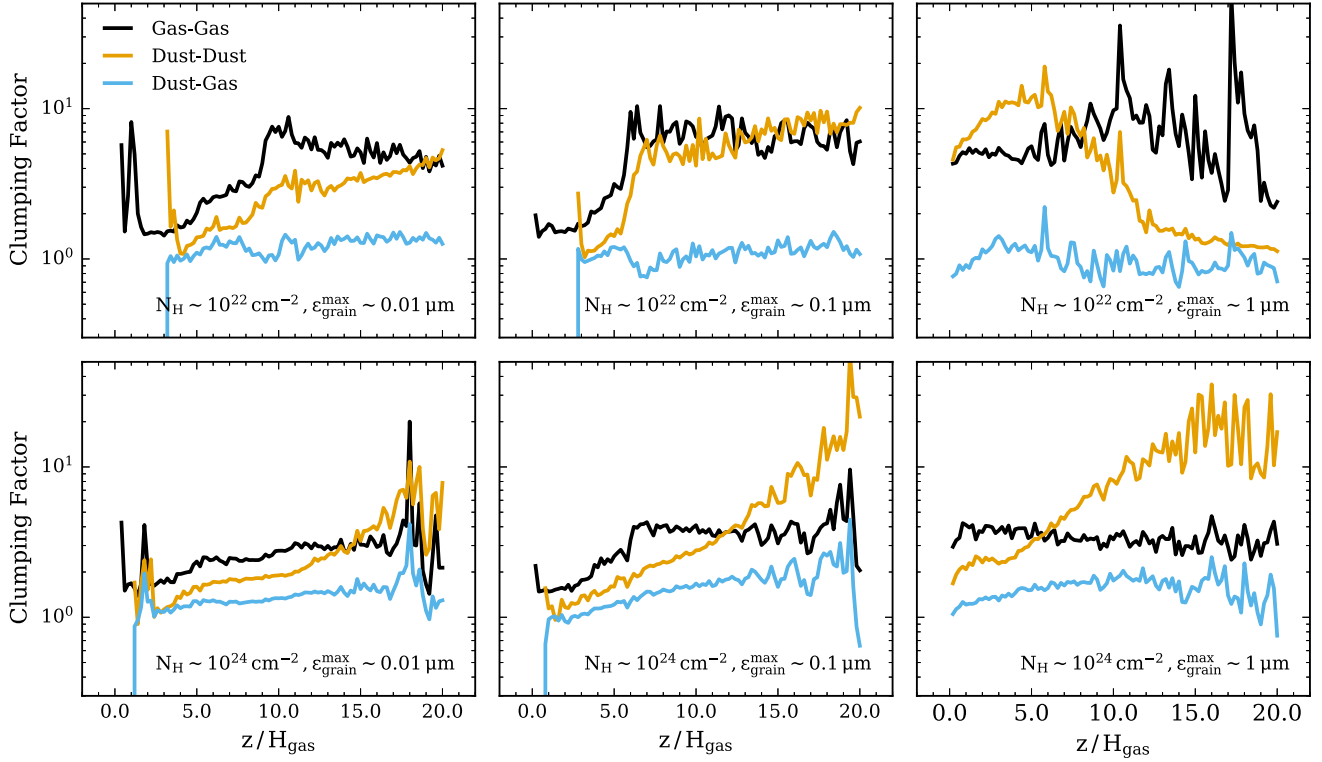


Figure 7. Clumping factors for gas–gas ($\langle \rho_g^2 \rangle / \langle \rho_g \rangle^2$), dust–dust ($\langle \rho_d^2 \rangle / \langle \rho_d \rangle^2$), and gas–dust ($\langle \rho_g \rho_d \rangle / \langle \rho_g \rangle \langle \rho_d \rangle$) at $t \sim \min(t_{\text{acc}}, t_{\text{esc}})$. From left to right, the maximum grain size $\epsilon_{\text{grain}}^{\text{max}}$ corresponds to 0.01, 0.1, and 1 μm , respectively, for an average column density of 10^{22}cm^{-2} (top) and 10^{24}cm^{-2} (bottom) within the simulation box. Gas–gas, dust–dust, and gas–dust clumping is significant near the centre of the wind where most of the mass resides. Further, dust–dust and gas–dust clumping is stronger for larger grains. For an extended discussion, refer to Section 4.4.

As a result, the dust distribution in the simulation shows more mass towards the bottom of the box, with a smaller amount of dust present at the top. The reason for this discrepancy is that the dust at the top has mostly escaped, while the majority of the dust remains concentrated at lower positions due to insufficient time to accelerate to higher positions. As a consequence, in this simulation, the clumping factors show an upward trend towards regions with higher dust density and decrease with height where there is less dust present.

In the general case, if we assume that C_{dd} is purely driven by the saturation of the RDIs, we expect clumping at some height z to be stronger where the RDI growth time at a given wavelength is shorter. Plugging in equilibrium values of w_s and t_s in the supersonic limit into equation (4), we obtain

$$t_{\text{grow}}(\lambda, z) \sim \left(\frac{\lambda^4 \rho_g e^{-z/H_{\text{gas}}} c_s^3}{a_{\text{eff}} \bar{\rho}_{\text{grain}}^i \epsilon_{\text{grain}} (\mu^{\text{dg}})^5} \right)^{1/6} \propto \rho_g e^{-z/6H_{\text{gas}}}. \quad (13)$$

As all the parameters in the expression above except for the stratified density term are roughly independent of height, we expect the RDI growth time-scale to get shorter as a function of height. In turn, the degree of dust clumping would increase as a function of height (clumping is approximately five times stronger for a factor ~ 10 increase in height) as shown in our plots. We note that this effect is suppressed for some of our simulations which could arise due to the non-linear evolution of the RDI's and/or competing processes such as turbulence.

In Fig. 8, we plot the zoomed-in column density profiles of the gas (top) and dust (bottom) in several RDMHD simulations. From left to right, the maximum grain size $\epsilon_{\text{grain}}^{\text{max}}$ corresponds to 0.01, 0.1,

and 1 μm , respectively, for an average column density of 10^{22}cm^{-2} within the simulation box. The structures formed appear more diffuse for smaller grain sizes. Usually, we see sharper structures for lower τ_{geo} , which could be shown by considering how t_{grow} depends on τ_{geo} . In equation (10), we showed that $t_{\text{acc}}/t_{\text{grow}} \propto \tau_{\text{geo}}^{-1/6}$, therefore environments with lower τ_{geo} would result in sharper structure.

As the micro-scale structure of the dust within the torus is not spatially resolved observationally, we cannot directly compare the structures formed within our simulations to observations. None the less, the physical variation in column densities could be inferred from the time variability for AGN sources. We discuss this in further detail in Section 5.1.

4.5 Evolution of velocity fluctuations

To further analyse the evolution of the resultant non-uniform internal structure of the outflows within our simulations, we explore velocity fluctuations in dust and gas here. It is important to note that there are multiple RDI modes present simultaneously within the simulation box, and while the short-wavelength modes will have the shortest growth times (Hopkins & Squire 2018b), the dynamics will be dominated by the large-scale modes, as well as non-linear effects and inhomogeneity in the wind (eg. different clumps/ filaments moving differently).

Figs 9 and 10 show the evolution of gas and dust turbulent velocity components. Fig. 9 displays the normalized root mean squared (RMS) random velocity dispersion for \hat{x} , \hat{y} , \hat{z} , and 3D components over time. Fig. 10 illustrates the normalized RMS velocity dispersion in the \hat{z} direction, σ_{vz} , and mean outflow velocity,

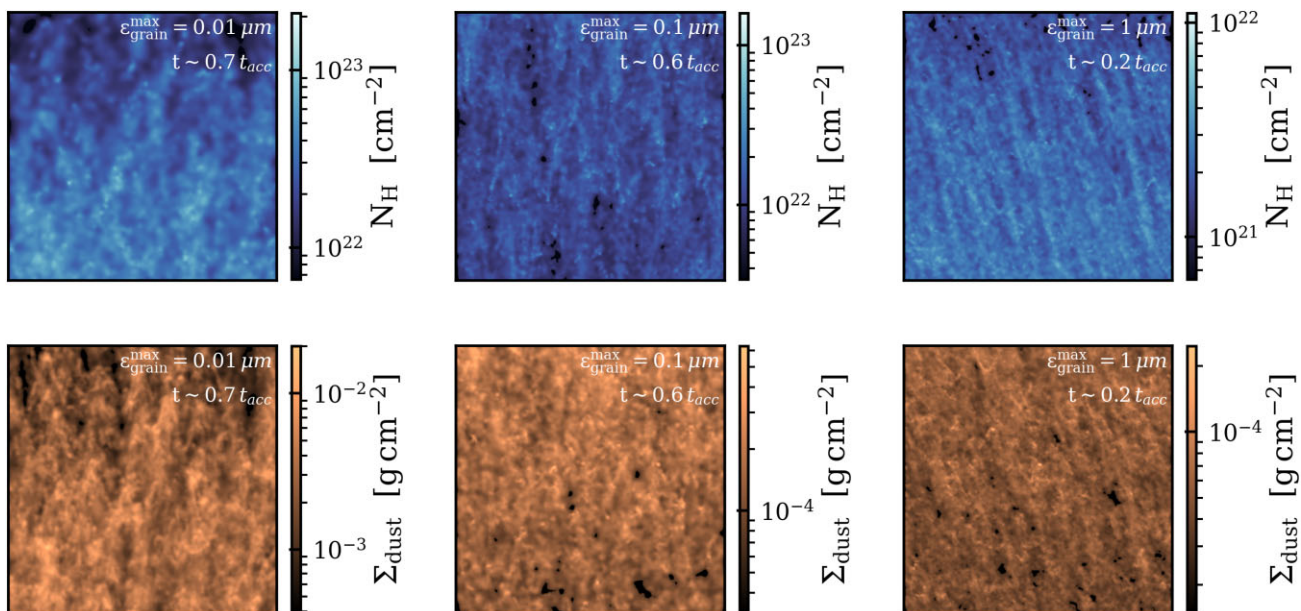


Figure 8. Gas column density (top) and dust surface density (bottom) within narrow bins in a zoomed-in region of high density within the AGN wind projected along the xz plane at $t \sim \min(t_{\text{acc}}, t_{\text{esc}})$ (where t_{esc} is the time at which 10 percent of the dust/gas has escaped the top of the box). From left to right, the maximum grain size $\epsilon_{\text{grain}}^{\text{max}}$ in the simulation box corresponds to 0.01, 0.1, and $1 \mu\text{m}$, respectively, for an average column density of 10^{22} cm^{-2} at times 0.7, 0.6, and $0.2 t_{\text{acc}}$. Note that as the absorption efficiency is grain-size-dependent, the dust surface density is proportional to the extinction with $A_{\lambda} \sim 0.1(\Sigma/10^{-4} \text{ g cm}^{-2})(\mu\text{m}/\epsilon_{\text{grain}}^{\text{max}})$. Larger grains show stronger clumping and thus more defined filaments.

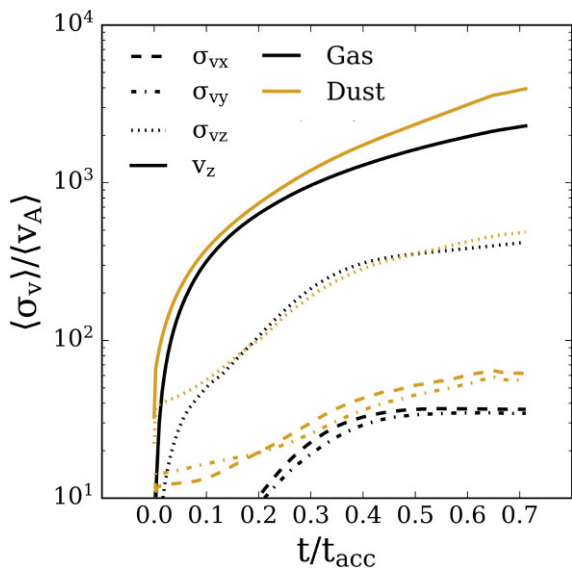


Figure 9. The temporal profile of the gas (black) and dust (yellow) velocity dispersion components (σ_{vx} , σ_{vy} , σ_{vz}) and outflow velocity v_z relative to the box averaged Alfvén speed (v_A), for a simulation box with $N_{\text{H}} \sim 10^{24} \text{ cm}^{-2}$, $\epsilon_{\text{grain}}^{\text{max}} \sim 1 \mu\text{m}$. The RMS random velocity dispersion quickly saturates in all directions for both the gas and the dust. The RMS dispersion is dominated by the \hat{z} -component (~ 10 per cent variation), i.e. the direction of the outflow, due to slightly different drift speeds for the gas, different dust sizes and different substructures. The \hat{x} and \hat{y} components are approximately one order of magnitude weaker.

v_z , as a function of height. The plot shows the behaviour for our $N_{\text{H}} \sim 10^{24} \text{ cm}^{-2}$, $\epsilon_{\text{grain}}^{\text{max}} \sim 1 \mu\text{m}$ run; however, we note that we observe the same behaviour throughout our parameter space. The dispersions grow exponentially fast (as expected if they are RDI-driven) at

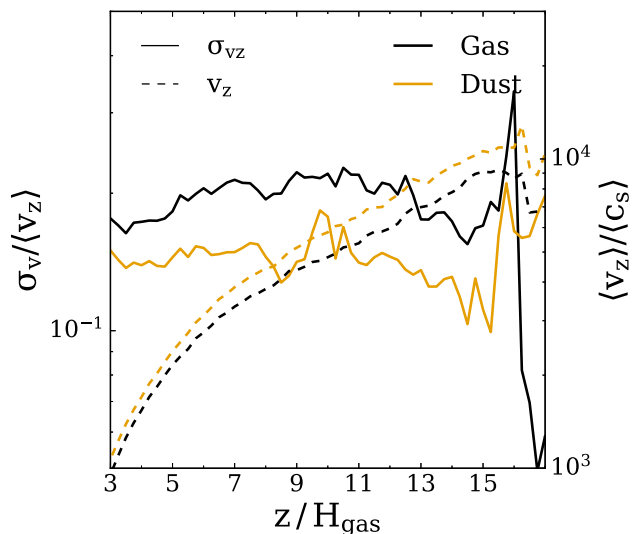


Figure 10. The spatial profile of the gas and dust random velocity dispersion (RMS) in the \hat{z} direction normalized to the average outflow velocity, (v_z) at a given height z , for a simulation box with $N_{\text{H}} \sim 10^{24} \text{ cm}^{-2}$, $\epsilon_{\text{grain}}^{\text{max}} \sim 1 \mu\text{m}$ at $t \sim 0.7 t_{\text{acc}}$. We also present the average flow velocity, (v_z), normalized to the average sound speed within the box, (c_s). The plot illustrates that the fluid (gas + dust) reaches highly supersonic velocities ($\sim 4 \times 10^4 \text{ km s}^{-1}$) and that the ratio of σ_{vz}/v_z remains relatively constant as a function of height within the box. We only show the \hat{z} -component of the dispersion in this plot as the \hat{x} and \hat{y} components show a similar behaviour but a magnitude weaker in the ratio of their respective velocity dispersion to the outflow velocity.

early stages and quickly saturate (within 0.1–0.2 t_{acc}) for all runs within our parameter set. This suggests that in an AGN tori, such instabilities have already saturated within the time taken to launch a wind, and later structure formation is mostly driven by radiation-

pressure accelerating the medium in addition to the turbulence within the flow.

Further, at the non-linear stage of their evolution, the gas and dust both reach similar super-Alfvénic random velocities with the RMS dispersion dominated by the \hat{z} -component. The \hat{x} and \hat{y} components are approximately one order of magnitude weaker due to the inherent geometry of the problem and the relatively weak Lorentz forces (i.e. $v \sim v_z \gg v_A$). As the turbulence is super-Alfvénic, the magnetic field has a weak influence on the flow dynamics, resulting in isotropic turbulence in the \hat{x} and \hat{y} directions as the magnetic field does not introduce significant anisotropy.

Analysing the spatial profile, we note ~ 20 per cent and ~ 2 per cent dispersion in the \hat{z} and $\hat{x} - \hat{y}$ directions, respectively, relative to the outflow velocity. Towards the base ($z \sim 0-3 H_{\text{gas}}$), and top ($z \sim 17-20 H_{\text{gas}}$) of the wind, the profile shows anomalous behaviour due to the presence of a relatively low number of dust particles/gas cells and boundary effects. Away from the boundaries, the dispersion shows no spatial dependence. In addition, we present the spatial profile of the outflow velocity, v_z , shown as a dashed line. We observe a consistent trend of increasing outflow velocity with height, as particles with higher velocities can travel further in a given time interval. Further, we note that the outflow attains highly supersonic velocities. Assuming an isothermal sound speed and a range of molecular gas temperatures in the range $T \sim 10^3-10^4$ K, we estimate that corresponds to a maximum outflow velocity range of $\sim 2-6 \times 10^4$ km s $^{-1}$. We compared our estimates with the observed velocities reported in Fiore et al. (2017) for AGNs with similar luminosities and find them to be consistent with X-ray winds with ultra-fast outflows. Therefore, while the comparison provides some insights, the velocities we observe in our simulations may not be directly comparable as they likely originate from different physical mechanisms and/or locations. However, as AGN outflows can arise from various physical processes, there are likely multiple mechanisms driving the observed outflows. Therefore, we caution against drawing definitive conclusions based solely on this comparison.

5 PREDICTED AGN VARIABILITY

5.1 Temporal and spatial variability in column densities along observed sight-lines

While it is difficult to resolve the underlying structure of the dust within AGN tori, AGN spectra and spectral energy distributions with high temporal resolution can be obtained which could probe these small-scale fluctuations. The methodology employed here closely follows that presented in Steinwandel et al. (2022) to which we refer for details. In Fig. 11, we compute the time variability in the sight-line-integrated surface density (Σ) of the dust and gas integrated for an infinitesimally narrow line of sight down the \hat{z} direction i.e. towards the accretion disc which should have an angular size that is very small compared to our resolution (hence an effectively infinitesimally narrow sight-line), and show the variance of the distribution in Fig. 12. From top to bottom, the total gas column density N_{H} in the simulation box corresponds to 10^{22} , 10^{24} , and 10^{26} cm $^{-2}$, respectively, and maximum grain size is $0.01 \mu\text{m}$ (left), and $0.1 \mu\text{m}$ (right). The plots show variability of the order of a few per cent for both the dust and gas over relatively short time-scales (a few years in physical units), and up to $\sim 20-60$ per cent variation on long time-scales (decades). The amplitude of the short-time-scale variations is roughly independent of maximum grain size and decreases for denser columns.

This result is consistent with our findings for the underlying morphological structure of the wind, where for low column density boxes with large grains, we find that the RDIs drive the formation of defined dense vertical filaments which would cause significant variability as they cross the line of sight. Further, the variability extends beyond the time taken for the instabilities to grow and is likely driven by the large velocity dispersion of the dust and gas. However, while the magnitude of the velocity dispersion is similar across all our runs, denser columns form more randomized clumps which are likely to be averaged over when integrating down the \hat{z} direction and thus result in weaker variation in the sight-line quantities compared to the 3D quantities (see e.g. Hopkins et al. 2022).

In principle, fluctuations in the integrated surface density could also exhibit corresponding fluctuations in the line-of-sight grain size distribution, as shown in the case of AGB-star outflows studied in Steinwandel et al. (2022). Therefore, we analyse the spatial fluctuations in the grain size distribution in the same manner as Σ . However, we find that the fluctuations in the grain size distribution are significantly weaker than the environments studied in Steinwandel et al. (2022) (perhaps consistent with our Σ fluctuations themselves being much weaker), and largely fall within the range we might expect from shot noise given our limited resolution (the shot noise being large for grain size fluctuations since we must consider only a narrow range of grain sizes, hence a more limited number of dust particles). Therefore, we cannot conclusively say whether or not there is a potentially measurable correlation between the fluctuations in Σ and the grain size distribution.

In Fig. 12, we show the spatial variability of the logarithmic gas and dust integrated surface densities computed over all possible sight-lines as a function of time. As one would expect, the variability in surface density increases as the RDIs develop. For lower column densities, the dust surface density shows higher variability for larger grain sizes. However, for simulations with column densities $N_{\text{H}} \gtrsim 10^{22}$ cm $^{-2}$, we observe a weak dependence of the surface density variation on the grain size, where the dust and gas exhibit similar levels of variation across different maximum grain sizes. Further, we note a trend of decreasing variation for increasing column densities. We are currently unaware of any significant observational constraints related to this particular trend. The lack of constraints can be attributed to the high column densities (Compton-thick) found in these environments and the predicted long time-scales on which variability occurs, spanning from decades to hundreds of years. Consequently, studying Compton-thick sources presents significant challenges. The anticipated variability in these sources is unlikely to be detected within the X-ray band, but it may manifest as a modulation of UV/IR radiation due to dust. Although this effect has not been disproven by observations, it is crucial to consider other factors, such as detailed cooling and heating physics, that could drive further variability within this regime. This underscores the need for further research to determine the primary sources of variability in Compton-thick environments. Therefore, for column densities of this magnitude, it is plausible that RDIs may not be the primary driver of variability.

To interpret the trend in the variability, we follow the analysis presented in Moseley et al. (2019). Assuming pure isothermal MHD turbulence, the variance of the gas density field will roughly follow a lognormal distribution of the form

$$\sigma^2(\ln(\rho_g)) = \ln \left(1 + (b|\sigma_v/c_s|)^2 \right), \quad (14)$$

where b corresponds to the ‘compressibility’ of the fluid with $b \sim 0.2-1$. We expect the saturation amplitude of the turbulence within

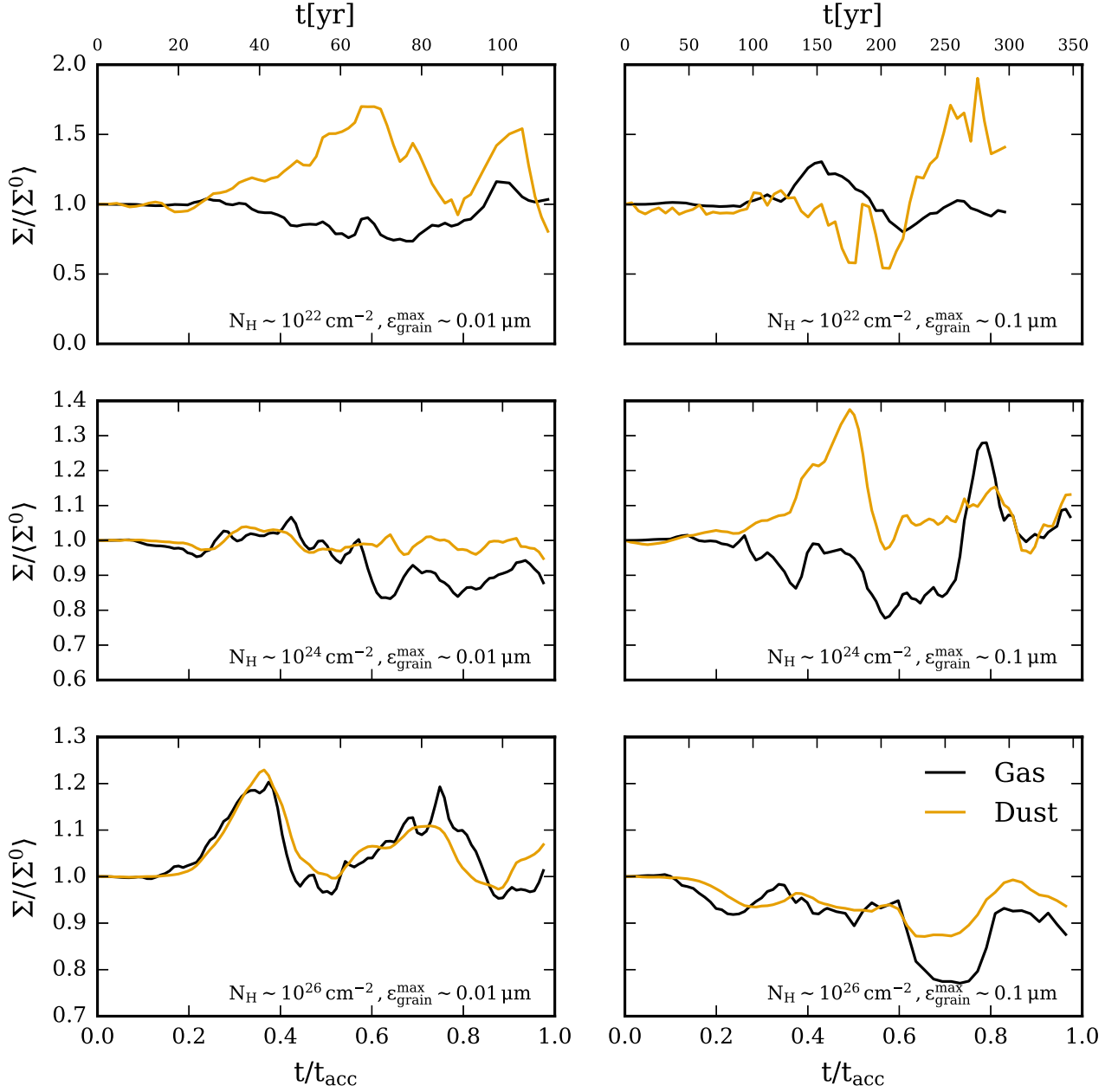


Figure 11. The sight-line-integrated surface density Σ along a random line of sight towards the AGN accretion disc. We normalize Σ to Σ^0 , the initial mean surface density in the simulation box for convenience. We compare both gas and dust columns, from top to bottom, the total gas column density N_{H} in the simulation box corresponds to 10^{22} , 10^{24} , and 10^{26} cm^{-2} , respectively, and maximum grain size is $0.01 \mu\text{m}$ (left), $0.1 \mu\text{m}$ (right). Overall, the dust and gas show fluctuations of similar amplitude, and there is an order of a few per cent variability on short time-scales (a few years), with higher variation (~ 10 – 40 per cent) on long time-scales relative to the acceleration time of the wind. However, at a given time the gas and dust Σ fluctuations do not exactly match.

the box to occur when the eddy turnover time-scale is of the order of the growth time-scale of the instability mode; this results in the following scaling for the long-wavelength regime:

$$\sigma_v \sim (\mu^{\text{dg}})^{1/3} (k \langle c_s \rangle \langle t_s \rangle)^{2/3} (\langle \mathbf{w}_s \rangle / c_s)^{2/3}. \quad (15)$$

Therefore, by combining both relations, we get

$$\sigma(\log(\rho_g)) \sim \ln \left(1 + \rho_g^{-4/3} \epsilon_{\text{grain}}^{1/3} \right). \quad (16)$$

So in the case where $\rho_g^{-4/3} \epsilon_{\text{grain}}^{1/3} \gg 1$, the variability will be higher for columns with lower density and larger grain sizes with a strong dependence on the density and a weak dependence on the grain

size. However, when $\rho_g^{-4/3} \epsilon_{\text{grain}}^{1/3} \ll 1$, the variability will be roughly similar at all densities and grain sizes.

In Fig. 13, we show the normalized probability density function (PDF) of the logarithmic surface density field for all times after the saturation of the RDIs and all sight-lines. From top to bottom, the total gas column density N_{gas} in the simulation box corresponds to 10^{22} and 10^{24} cm^{-2} , respectively, and maximum grain size is $0.01 \mu\text{m}$ (left), $0.1 \mu\text{m}$ (middle), and $1 \mu\text{m}$ (right). We omit the plots for larger column densities but report that they are similar to the bottom left plot. As shown in the plots, the profile of the PDFs is highly non-Gaussian with a narrow peaked core component and wings that sharply drop off, indicative of strongly enhanced fluctuations. The

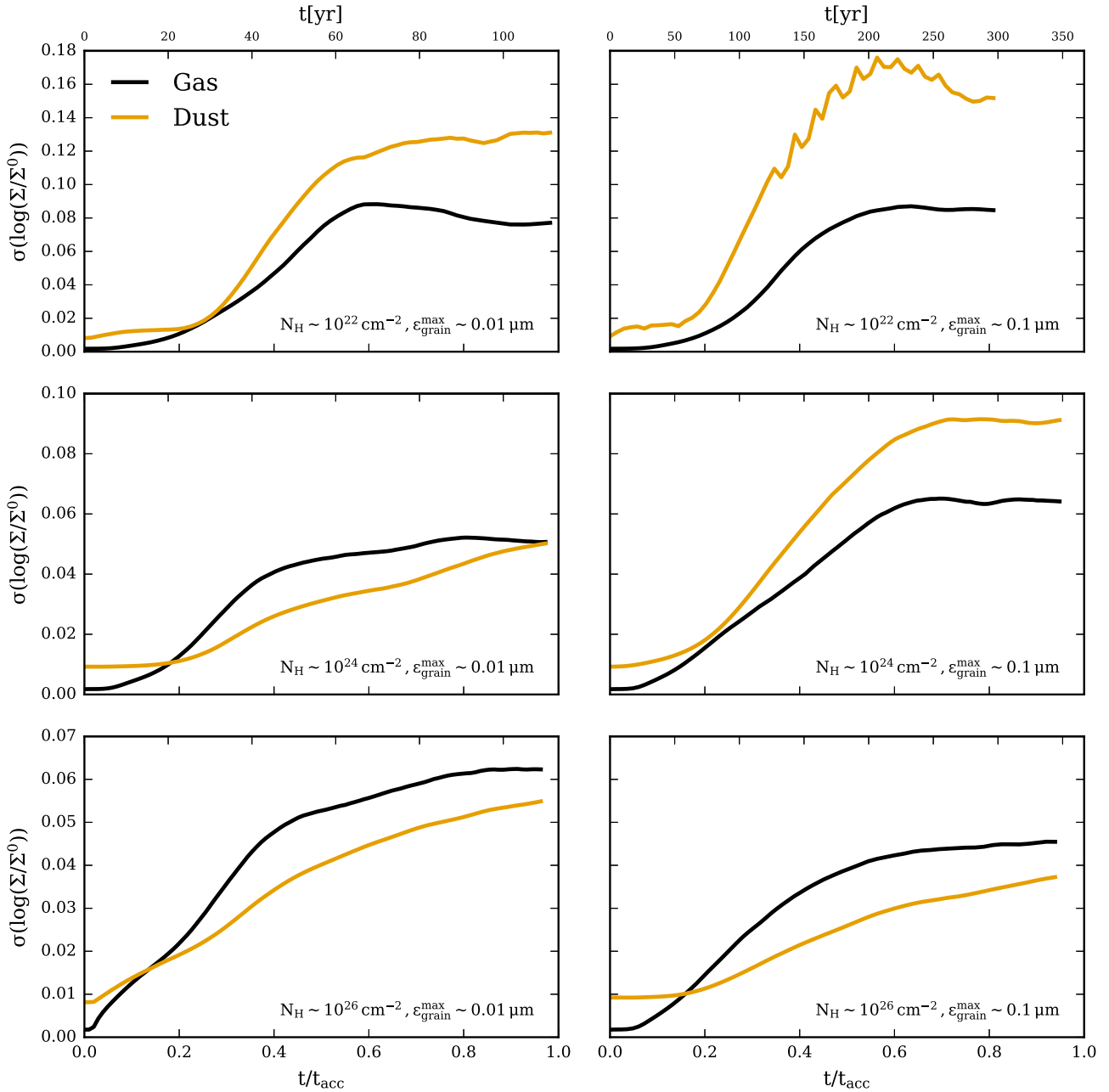


Figure 12. The sight-line-to-sight-line spatial variability of the gas and dust integrated surface densities across different sight-lines within the box as a function of time. We specifically plot 1σ dispersion in the log of the surface density compared across 100 random sight-lines to the AGN accretion disc, through the wind, at each time t . From top to bottom, the total gas column density N_{H} in the simulation box corresponds to 10^{22} , 10^{24} , and 10^{26} cm^{-2} , respectively, and maximum grain size is $0.01 \mu\text{m}$ (left), and $0.1 \mu\text{m}$ (right). Both the gas and the dust show similar degrees of variability, with the dust variability increasing at a higher rate at later times. We note that below $N_{\text{H}} \sim 10^{26} \text{ cm}^{-2}$, larger grains result in a larger variation due to more prominent vertical filaments across the simulation; however, the grain size has a minimal effect on the spread of the distribution for higher column densities.

dust PDF is broader than that of the gas at lower column densities and higher grain sizes, i.e. when the dust is not well coupled with the gas. This difference is negligible for more obscured lines of sight ($N_{\text{H}} \gtrsim 10^{24} \text{ cm}^{-2}$), as the fluid is strongly coupled across the range of grain sizes we consider.

5.1.1 Power spectral analysis

In Fig. 14, we present the temporal power spectrum, for individual lines of sight (as Fig. 2) and averaged over all lines of sight, of the

integrated gas and dust surface density in black and yellow thick lines, respectively. We show this for a simulation with $N_{\text{H}} \sim 10^{24} \text{ cm}^{-2}$ and $\epsilon_{\text{grain}}^{\text{max}} \sim 0.01 \mu\text{m}$. We omit the spectra for the remainder of our simulation set as they show a similar profile. The spectra for dust and gas show similar profiles, with twice the amount of power present in the dust spectrum relative to the gas (consistent with our previous analysis). The plot indicates that most of the power is on long time-scales, with a spectral index $\alpha_{\nu} \sim -2$, defined as $dP/d\nu \propto \nu^{\alpha_{\nu}}$. This spectral index is very close to canonical red noise which is consistent with AGN observations probing comparable time-scales (MacLeod

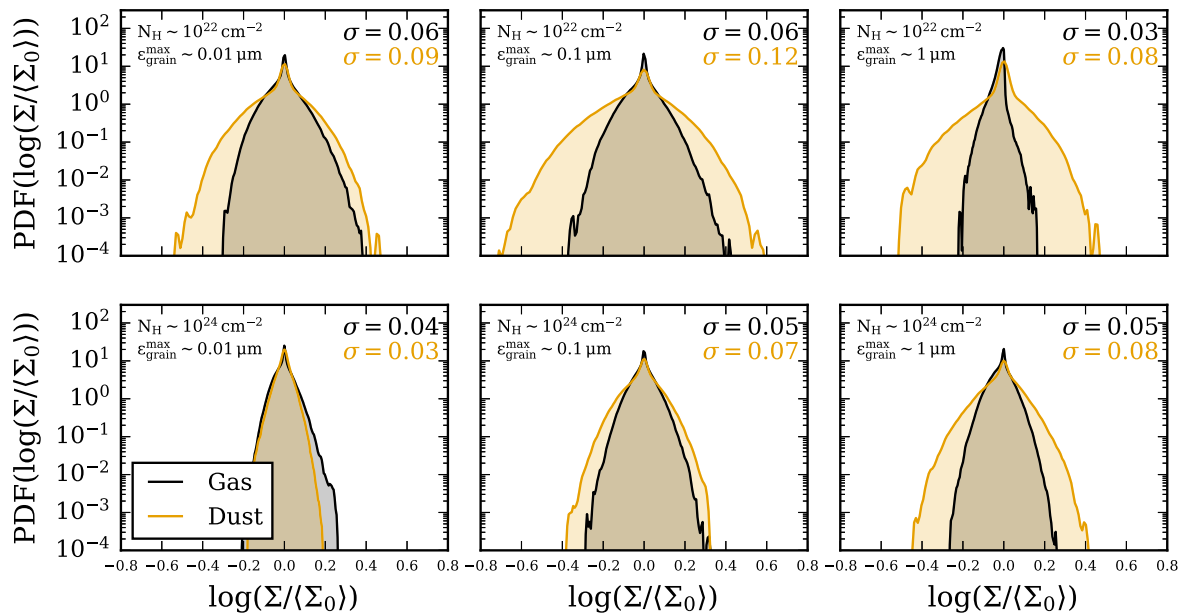


Figure 13. The normalized PDF of the surface density for the dust and gas components across 100 random sight-lines at each time, combining all times after the wind begins to launch ($t > 0.1t_{\text{acc}}$). From top to bottom, the total gas column density N_{H} in the simulation box corresponds to 10^{22} and 10^{24} cm^{-2} , and maximum grain size is $0.01 \mu\text{m}$ (left), $0.1 \mu\text{m}$ (middle), and $1 \mu\text{m}$ (right). The PDFs show distributions that are highly non-Gaussian with a narrow peaked core component and wings with steep drop-offs as a result of enhanced fluctuations. On average, the dust shows a higher spread in the distribution than the gas as expected given its collisionless nature. This difference in spread decreases as the fluid approaches the limit of being perfectly coupled, i.e. smaller grain sizes, and higher column densities, again as expected for the RDI's.

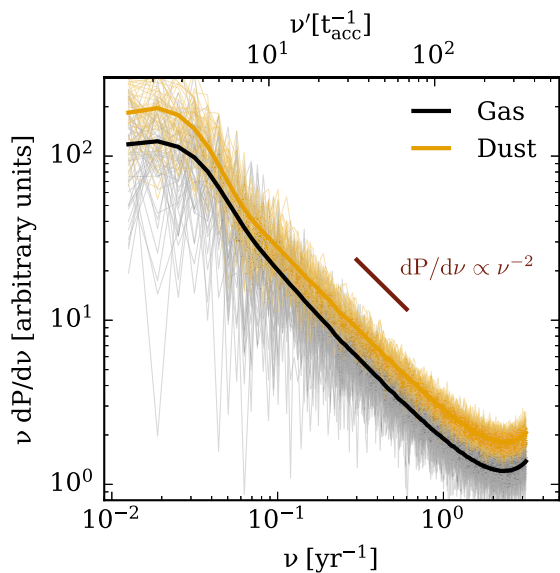


Figure 14. Temporal power spectrum of the gas and dust sight-line-integrated surface densities along individual sight-lines as Fig. 11. The thick lines show the average over all sight-lines. This is for one RDMHD simulation with initial $N_{\text{H}} \sim 10^{24}$ cm^{-2} and $\epsilon_{\text{grain}}^{\text{max}} \sim 0.01 \mu\text{m}$, but others are qualitatively similar. Both the dust and gas show similar profiles, with the dust carrying roughly twice the amount of power as the gas. The spectra show power with an approximate red-noise spectrum, $dP/d\nu \propto \nu^{-2}$, over most of the resolvable time range. We expect that the power on long time-scales is mostly driven by global processes such as the vertical acceleration of the fluid and that the power on shorter time-scales is driven by the density fluctuations in the wind.

et al. 2012; Caplar et al. 2017), and could arise from an array of physical processes. For instance, if we assume that on small scales, the density fluctuations take the form of a Gaussian random field, as the surface density is an integral over that field, it is natural that the resulting power spectrum would take this form. However, it is worth noting that observations of optical power spectral densities have indicated a range of slopes, with values often steeper than the canonical -2 value at high frequencies (Simm et al. 2016; Smith et al. 2018).

Further, we note a break at the low-frequency end of the power spectrum, which corresponds to the acceleration time-scale of the fluid within the simulation box. Similar breaks have been observed in AGN power spectra, which were found to be correlated with intrinsic properties of AGNs such as their mass (Burke et al. 2021). However, these breaks were observed to occur on different time-scales compared to the breaks in our simulations. The high-frequency plateau in our PSD, however, is likely an artefact due to our limited time resolution and simulation duration. Overall, we acknowledge the complexity and variability of AGN power spectra and caution readers about the limitations of our simulations in capturing the full range of observed power spectrum behaviours.

In Fig. 15, we show the spatial power spectrum of the logarithm of the three-dimensional density field for a column with $N_{\text{H}} \sim 10^{24}$ cm^{-2} and $\epsilon_{\text{grain}}^{\text{max}} \sim 0.01 \mu\text{m}$, and similar to above, note that it is roughly consistent with the spectra for our other simulations. The plot shows similar profiles for the dust and the gas, which is indicative that on the relatively large scales that we are probing, the dust and gas fluctuations are order-of-magnitude comparable. Further, the power increases exponentially with a spectral index $\alpha_k \sim 3$, defined as $dP/dk \propto k^{\alpha_k}$ until a few factors of the resolution limit is hit, after which power on smaller length-scales would not be resolvable. Thus, the power decay on relatively short-length-scales should be regarded

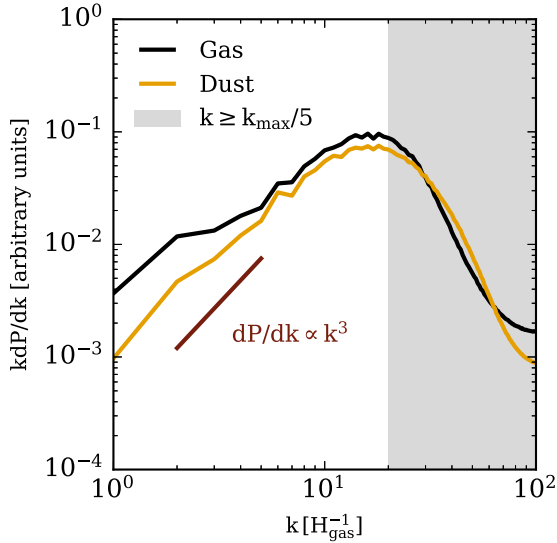


Figure 15. Spatial power spectrum of the three-dimensional dust and gas log density fields ($\log(\rho_{\text{gas}} / \langle \rho_{\text{gas}} \rangle)$), ($\log(\rho_{\text{dust}} / \langle \rho_{\text{dust}} \rangle)$). We show this for one simulation with $N_{\text{H}} \sim 10^{24} \text{ cm}^{-2}$ and $\epsilon_{\text{grain}}^{\text{max}} \sim 0.01 \mu\text{m}$ at $t \sim t_{\text{acc}}$, but others are qualitatively similar. The plot shows similar power for the gas and dust that increases on small scales roughly according to $dP/dk \propto k^3$ until the resolution limit is approached (k_{max} corresponds to the simulation resolution limit), after which due to numerical effects, power on smaller length-scales decreases as modes are unresolved.

as a numerical effect, as we expect it to continue to rise for smaller length-scales.

5.1.2 Relation to AGN observations

The RDIs and other instabilities provide a natural explanation for the clumpy nature of the dusty torus, which together with the turbulent dynamics of the fluid results in variability in the observed luminosity. While the variation we deduce is relatively small, it is non-negligible. We resolve ~ 10 – 30 per cent variation on scales of a few years which would be observable on human time-scales. For Compton-thick sources, such variability in the gas column would be detectable and significantly change the hardness of the observed X-rays and reduce luminosity by factors of ~ 2 . However, the typical behaviour in our simulations would not give rise to variability similar to more extreme changing-look AGNs, which presumably is due to other physics (e.g. accretion disc state changes).

We compare our results to optical variability studies by MacLeod et al. (2010), Suberlak, Ivezić & MacLeod (2021), and Stone et al. (2022). These studies report similar PSD slopes of -2 , consistent absolute magnitude variability amplitudes, and characteristic break time-scales on the order of years. While our simulations predict variability that extends to longer time-scales and longer break time-scales, determining such time-scales would require longer observational baselines. Additionally, we take note of the X-ray variability observations by Gonzalez-Martin & Vaughan (2012), which also exhibit consistency with red noise characteristics. However, we acknowledge that X-ray variability is likely dominated by processes occurring in the accretion disc and operates on much shorter time-scales. Therefore, while there is a similarity in the power spectrum slopes, it may not be the most suitable comparison for our simulations. While our model matches the reported PSDs in shape and magnitude, caution is advised in overgeneralizing the agreement. Red noise spectra can stem from widespread Gaussian

processes, suggesting that other mechanisms are likely contributing to the observed variability.

For our model, we expect the primary source of obscuration at optical/UV wavelengths to be the dust component, while at shorter wavelengths such as X-rays, we anticipate that gas will dominate the obscuration. A unique feature of our model is that it predicts a correlation between the variability at different wavelengths, with RDIs driving simultaneous variability at varying magnitudes depending on the observation wavelength. Therefore, the extinction at a given wavelength, A_{λ} , would be proportional to the dust surface density, $\delta \Sigma_{\text{dust}}$, and related by the extinction coefficient, K_{λ} , i.e. $\delta A_{\lambda} \sim K_{\lambda} \cdot \delta \Sigma_{\text{dust}}$. Based on previous estimates by Draine (2003), we expect values of K_{λ} to be around 5–10 in the optical band and 0.5–5 in the IR band. However, our simulations do not include the region interior to the sublimation radius often associated with AGN X-ray variability (Merloni et al. 2014; Middei et al. 2017). As this region is dust-free, any variability attributed to that region cannot be driven by the RDIs.

For our simulations, we predict several distinctive features that differentiate them from other models. One such feature is the relative variation between the dust and gas components. We observe fluctuations in the line-of-sight integrated dust-to-gas ratio, where the dust component varies independently of the gas component and sometimes in opposite directions. Observationally, this would manifest as instances where the UV spectrum becomes highly reddened due to increased dust obscuration, while the X-ray spectrum remains relatively constant, or vice versa. Additionally, variations in the dust-to-gas ratio would introduce variability in the observed extinction curve. Similar variability has been reported by Dahmer-Hahn et al. (2023), which reports variability on decade time-scales in the near-infrared (NIR) that does not correlate with the observed variability in X-ray gas reported by Sanfrutos et al. (2016) in regions corresponding to the dusty torus. Furthermore, there have been observations of sources where the X-ray flux varies by approximately 20 per cent to 80 per cent over a few years, with no apparent variation in the optical component (Risaliti et al. 2002, 2005; De Rosa et al. 2007; Markowitz et al. 2014; Laha et al. 2020). Another feature predicted by our RDI simulations is the presence of high-velocity outflows that surpass the Keplerian velocity of the region. Observations by Choi et al. (2022) in the AGN torus region have reported broad absorption lines corresponding to torus-like distances from the AGN source, indicating the presence of such high-velocity outflows that align with the predictions from our RDI model. However, if other mechanisms drive similar changes in the dust-to-gas ratio or high-velocity outflows, the observed variations may become degenerate, making it challenging to attribute the variability solely to the RDI mechanism.

In addition to that, we caution that our findings are sensitive to both the physical size of the line-of-sight/spatial resolution and the temporal resolution of our simulations. When considering observations, the thickness of the line of sight is limited by the size of the emitting region, i.e. the angular size of the AGN disc. Therefore, to validate our choice of an infinitesimally narrow line of sight for our calculations, we consider the size of the AGN disc relative to the size of the torus. An AGN of luminosity $10^{46} \text{ erg s}^{-1}$ with a disc emitting black-body radiation peaking in the near-UV regime with an effective temperature of $\sim 10^4 \text{ K}$ will have a radius, R_{d} of order $R_{\text{d}} \sim \sqrt{L/4\pi\sigma_{\text{SB}}T^4} \sim 3 \times 10^{-2} \text{ pc}$, where σ_{SB} is the Stefan–Boltzmann constant. Therefore, for torus of radius $\sim 1 \text{ pc}$, an infinitesimally narrow line of sight would be a reasonable approximation to an observationally limited line of sight. However, there have been cases where the continuum emission region has been resolved in the UV/IR waveband (Leighly et al. 2019).

Regarding the time-scales of the variability predicted by our analysis, we note that the shortest time-scales we can resolve are limited by the frequency at which we output our snapshots (\sim years), therefore we are not resolving variability on all human observable time-scales and would expect that there would still be variability due to the RDIs on shorter time-scales than those reported in this work. In addition, we expect that the variability that arises due to the RDIs would be much faster than that predicted by an occultation model.

6 CONCLUSIONS

In this work, we present simulations of radiation-dust-driven outflows explicitly accounting for dust dynamics and dust–gas radiation-magnetic field interactions, with initial conditions resembling AGN tori. We model the dust using a realistic grain size spectrum and grain charge under the influence of a radiation field and accounting for drag and Lorentz forces. The dust interacts with gas through collisional (drag) and electromagnetic (Lorentz, Coulomb) forces, which couple the two fluids and absorb the radiation which accelerates grains, determining whether they, in turn, can accelerate gas. While within this environment, the dust and gas are closely coupled in the sense that the ‘free streaming length’ of dust grains is very small, explicit treatment of dust dynamics reveals that the fluid is unstable on all length-scales to a broad spectrum of fast-growing instabilities. We summarize our key findings below.

(i) **RDIs:** The RDIs develop rapidly on scales up to the box size, forming vertical filamentary structures that reach saturation quickly relative to global time-scales. We find that the behaviour of the RDIs is sensitive to the geometrical optical depth τ_{geo} with environments with higher optical depths resulting in a more tightly coupled dust–gas fluid ($\ell_{\text{stream,dust}}/H_{\text{gas}} \propto \tau_{\text{geo}}^{-1}$ as shown in equation (6)), and longer RDI growth times ($t_{\text{grow}}/t_{\text{acc}} \propto \tau_{\text{geo}}^{1/6}$ as shown in equation (10)). Other parameters such as AGN luminosity, gravity, grain charging mechanism, and the gaseous equation of state show weaker effects on the dynamics or morphology of the RDIs.

(ii) **Clustering:** The RDIs drive strong dust–dust and gas–gas clustering of similar magnitude (order of magnitude fluctuations) on small scales for all conditions explored within our parameter set. Thus, the RDIs provide yet another (of many) natural mechanism for explaining the clumpy nature of AGN tori.

(iii) **Outflows:** Our results show that both the dust and gas are accelerated to highly supersonic velocities resulting in a wind which can successfully eject 70–90 per cent of the gas present. In addition, the RDIs drive super-Alfvénic velocity dispersion of order ~ 10 per cent of the outflow velocity. Further, while the morphological structure of the RDIs generates low-opacity channels through which photons can in principle escape, we find that this ‘leakage’ is modest, usually resulting in less than a factor of ~ 3 loss of photon momentum relative to the ideal case. In every case, the remaining momentum (for quasar-like conditions modelled here) is more than sufficient to drive a wind.

(iv) **Integrated surface density variation:** The resulting morphology and turbulence give rise to both short (\leq years) and long time-scale (10–100 yr) variability in the column density of gas and surface density/opacity of dust integrated along mock observed lines of sight to the quasar accretion disc. These fluctuations have RMS amplitude along a given sight-line of order ~ 10 –20 per cent over year to decade time-scales with a red noise power spectrum, consistent with a wide array of AGN observations. We note that both the dust and gas show variability on similar time-scales that roughly follow similar trends statistically, but do not match one-to-one at

any given time – they fluctuate relative to one another, providing a natural explanation for systems where dust extinction is observed to vary in the optical/NIR independent of the gas-dominated X-ray obscuration and vice versa (Risaliti et al. 2002, 2005; De Rosa et al. 2007; Smith & Vaughan 2007; Markowitz et al. 2014; Laha et al. 2020). Our model suggests that the variability in the optical/NIR bands will be correlated in time and proportional to the variability in dust surface density. The X-ray variability, which is associated with the gas surface density variation caused by RDIs, is not expected to be strongly correlated with the optical/NIR variability.

ACKNOWLEDGEMENTS

Support for NS and PFH was provided by NSF Research Grants 1911233, 20009234, 2108318, NSF CAREER grant 1455342, NASA grants 80NSSC18K0562, HST-AR-15800. Numerical calculations were run on the Caltech compute cluster ‘Wheeler’, allocations AST21010 and AST20016 supported by the NSF and TACC, and NASA HEC SMD-16-7592.

DATA STATEMENT

The data supporting this article are available on reasonable request to the corresponding author.

REFERENCES

- Alonso-Herrero A. et al., 2011, *ApJ*, 736, 82
 Alonso-Herrero A. et al., 2021, *A&A*, 652, A99
 Antonucci R. R. J., 1982, *Nature*, 299, 605
 Apai D. A., Lauretta D. S., 2010, in Apai D., Lauretta D. S., eds, *Protoplanetary Dust: Astrophysical and Cosmochemical Perspectives*. Cambridge Univ. Press, Cambridge, UK
 Arakawa N., Fabian A., Ferland G., Ishibashi W., 2022, *MNRAS*, 517, 5069
 Asmus D., Hoenig S. F., Gandhi P., 2016, *ApJ*, 822, 109
 Assef R. et al., 2018, *ApJ*, 866, 26
 Bai X.-N., Stone J. M., 2010, *ApJ*, 722, L220
 Baloković M. et al., 2018, *ApJ*, 854, 42
 Banerji M., McMahon R. G., Hewett P. C., Alaghband-Zadeh S., Gonzalez-Solares E., Venemans B. P., Hawthorn M. J., 2012, *MNRAS*, 427, 2275
 Baskin A., Laor A., 2018, *MNRAS*, 474, 1970
 Bendo G. et al., 2010, *A&A*, 518, L65
 Bianchi S., Piconcelli E., Chiaberge M., Bailón E. J., Matt G., Fiore F., 2009, *ApJ*, 695, 781
 Burke C. J. et al., 2021, *Science*, 373, 789
 Burtscher L. et al., 2016, *A&A*, 589, A130
 Caplar N., Lilly S. J., Trakhtenbrot B., 2017, *ApJ*, 834, 111
 Carballido A., Stone J. M., Turner N. J., 2008, *MNRAS*, 386, 145
 Chan C.-H., Krolik J. H., 2016, *ApJ*, 825, 67
 Choi H., Leighly K. M., Terndrup D. M., Dabbieri C., Gallagher S. C., Richards G. T., 2022, *ApJ*, 937, 74
 Costa T., Rosdahl J., Sijacki D., Haehnelt M. G., 2018, *MNRAS*, 473, 4197
 Dahmer-Hahn L. G., Rodríguez-Ardila A., Bianchin M., Riffel R. A., Riffel R., Storchi-Bergmann T., Hao L., 2023, *MNRAS*, 523, 5502
 De Rosa A., Piro L., Perola G., Capalbi M., Cappi M., Grandi P., Maraschi L., Petrucci P., 2007, *A&A*, 463, 903
 Debuhr J., Quataert E., Ma C., Hopkins P., 2010, *MNRAS*, 406, L55
 Dorschner J., 2003, in Henning T. K. ed., *Lecture Notes in Physics*, Vol. 609, *Astromineralogy*. Springer-Verlag, Berlin, p. 1
 Draine B. T., 2003, *ARA&A*, 41, 241
 Draine B. T., Lee H. M., 1984, *ApJ*, 285, 89
 Draine B. T., Sutin B., 1987, *ApJ*, 320, 803
 Draine B. et al., 2007, *ApJ*, 663, 866
 Dwek E., 1998, *ApJ*, 501, 643
 Elitzur M., Shlosman I., 2006, *ApJ*, 648, L101

- Elvis M., 2000, *ApJ*, 545, 63
- Elvis M., Marengo M., Karovska M., 2002, *ApJ*, 567, L107
- Esparza-Arredondo D., Gonzalez-Martín O., Dultzin D., Masegosa J., Ramos-Almeida C., García-Bernete I., Fritz J., Osorio-Clavijo N., 2021, *A&A*, 651, A91
- Fiore F. et al., 2017, *A&A*, 601, A143
- Fluetsch A. et al., 2018, *MNRAS*, 483, 4586
- Gallerani S. et al., 2010, *A&A*, 523, A85
- García-Bernete I. et al., 2022, *A&A*, 667, A140
- Glikman E. et al., 2012, *ApJ*, 757, 51
- Gonzalez-Martin O., Vaughan S., 2012, *A&A*, 544, A80
- Groves B. A., Heckman T. M., Kauffmann G., 2006, *MNRAS*, 371, 1559
- Grudić M. Y., Guszejnov D., Hopkins P. F., Offner S. S. R., Faucher-Giguère C.-A., 2021, *MNRAS*, 506, 2199
- Hamann F., Korista K., Ferland G. J., Warner C., Baldwin J., 2002, *ApJ*, 564, 592
- Hatziminaoglou E., Fritz J., Jarrett T., 2009, *MNRAS*, 399, 1206
- Hickox R. C., Alexander D. M., 2018, *ARA&A*, 56, 625
- Hoening S. F., Beckert T., 2007, *MNRAS*, 380, 1172
- Höfner S., Olofsson H., 2018, *A&AR*, 26, 1
- Hon W. J., Webster R., Wolf C., 2020, *MNRAS*, 497, 192
- Hönig S. F., 2019, *ApJ*, 884, 171
- Hönig S. F., Kishimoto M., 2010, *A&A*, 523, A27
- Hönig S. F., Kishimoto M., 2017, *ApJ*, 838, L20
- Hopkins P. F., 2015, *MNRAS*, 450, 53
- Hopkins P. F., 2016, *MNRAS*, 462, 576
- Hopkins P. F., 2017, *MNRAS*, 466, 3387
- Hopkins P. F., Grudić M. Y., 2019, *MNRAS*, 483, 4187
- Hopkins P. F., Lee H., 2016, *MNRAS*, 456, 4174
- Hopkins P. F., Raives M. J., 2016, *MNRAS*, 455, 51
- Hopkins P. F., Squire J., 2018a, *MNRAS*, 479, 4681
- Hopkins P. F., Squire J., 2018b, *MNRAS*, 480, 2813
- Hopkins P. F. et al., 2004, *AJ*, 128, 1112
- Hopkins P. F., Grudić M. Y., Wetzel A., Kereš D., Faucher-Giguère C.-A., Ma X., Murray N., Butcher N., 2020a, *MNRAS*, 491, 3702
- Hopkins P. F., Squire J., Seligman D., 2020b, *MNRAS*, 496, 2123
- Hopkins P. F., Rosen A. L., Squire J., Panopoulou G. V., Soliman N. H., Seligman D., Steinwandel U. P., 2022, *MNRAS*, 517, 1491
- Horst H., Gandhi P., Smette A., Duschl W. J., 2008, *A&A*, 479, 389
- Isbell J. W. et al., 2022, *A&A*, 663, A35
- Ishibashi W., Fabian A. C., 2015, *MNRAS*, 451, 93
- Ishibashi W., Fabian A. C., Maiolino R., 2018, *MNRAS*, 476, 512
- Ivezić Ž., Elitzur M., 1997, *MNRAS*, 287, 799
- James A., Dunne L., Eales S., Edmunds M. G., 2002, *MNRAS*, 335, 753
- Ji S., Squire J., Hopkins P. F., 2022, *MNRAS*, 513, 282
- Johansen A., Youdin A., Mac Low M.-M., 2009, *ApJ*, 704, L75
- Kawakatu N., Wada K., Ichikawa K., 2020, *ApJ*, 889, 84
- King A., Pounds K., 2015, *ARA&A*, 53, 115
- Kishimoto M., Hönig S. F., Antonucci R., 2009, *ApJ*, 697, L69
- Kishimoto M., Hönig S. F., Antonucci R., Barvainis R., Kotani T., Tristram K. R. W., Weigelt G., Levin K., 2011a, *A&A*, 527, A121
- Kishimoto M., Hönig S. F., Antonucci R., Millour F., Tristram K. R., Weigelt G., 2011b, *A&A*, 536, A78
- Konigl A., Kartje J. F., 1994, *ApJ*, 434, 446
- Krolik J. H., Begelman M. C., 1988, *ApJ*, 329, 702
- Krumholz M. R., Thompson T. A., 2012, *ApJ*, 760, 155
- Kuiper R., Klahr H., Beuther H., Henning T., 2012, *A&A*, 537, A122
- LaMassa S. M. et al., 2015, *ApJ*, 800, 144
- Laha S., Markowitz A. G., Krumpke M., Nikutta R., Rothschild R., Saha T., 2020, *ApJ*, 897, 66
- Laor A., Draine B. T., 1993, *ApJ*, 402, 441
- Lawrence A., 1991, *MNRAS*, 252, 586
- Lawrence A., Elvis M., 1982, *ApJ*, 256, 410
- Lee H., Hopkins P. F., Squire J., 2017, *MNRAS*, 469, 3532
- Leighly K. M., Cooper E., Grupe D., Terndrup D. M., Komossa S., 2015, *ApJ*, 809, L13
- Leighly K. M., Terndrup D. M., Lucy A. B., Choi H., Gallagher S. C., Richards G. T., Dietrich M., Raney C., 2019, *ApJ*, 879, 27
- Lissauer J. J., 1993, *ARA&A*, 31, 129
- Liu B., Ji J., 2020, *Res. Astron. Astrophys.*, 20, 164
- Lupi A., Volonteri M., Silk J., 2017, *MNRAS*, 470, 1673
- Lupi A., Bovino S., Capelo P. R., Volonteri M., Silk J., 2018, *MNRAS*, 474, 2884
- MacLeod C. L. et al., 2010, *ApJ*, 721, 1014
- MacLeod C. L. et al., 2012, *ApJ*, 753, 106
- Magrini L. et al., 2011, *A&A*, 535, A13
- Maiolino R., Marconi A., Salvati M., Risaliti G., Severgnini P., Oliva E., La Franca F., Vanzani L., 2001, *A&A*, 365, 28
- Maiolino R., Schneider R., Oliva E., Bianchi S., Ferrara A., Mannucci F., Pedani M., Roca Sogorb M., 2004, *Nature*, 431, 533
- Markowitz A., Krumpke M., Nikutta R., 2014, *MNRAS*, 439, 1403
- Mathis J. S., 1990, *ARA&A*, 28, 37
- Mathis J. S., Rimpl W., Nordsieck K. H., 1977, *ApJ*, 217, 425
- Mathur S. u. et al., 2018, *ApJ*, 866, 123
- McElroy R. et al., 2016, *A&A*, 593, L8
- McKinnon R., Vogelsberger M., Torrey P., Marinacci F., Kannan R., 2018, *MNRAS*, 478, 2851
- Merloni A. et al., 2014, *MNRAS*, 437, 3550
- Midde R., Vagnetti F., Bianchi S., La Franca F., Paolillo M., Ursini F., 2017, *A&A*, 599, A82
- Minisale M., Dulieu F., Cazaux S., Hocuk S., 2016, *A&A*, 585, A24
- Moseley E. R., Squire J., Hopkins P. F., 2019, *MNRAS*, 489, 325
- Murray N., Quataert E., Thompson T. A., 2005, *ApJ*, 618, 569
- Nenkova M., Sirocky M. M., Ivezić Ž., Elitzur M., 2008a, *ApJ*, 685, 147
- Nenkova M., Sirocky M. M., Nikutta R., Ivezić Ž., Elitzur M., 2008b, *ApJ*, 685, 160
- Netzer H., 2015, *ARA&A*, 53, 365
- Padovani P. et al., 2017, *A&AR*, 25, 2
- Pan L., Padoan P., Scalo J., Kritsuk A. G., Norman M. L., 2011, *ApJ*, 740, 6
- Paolillo M., Schreier E., Giacomoni R., Koekemoer A., Grogin N., 2004, *ApJ*, 611, 93
- Paolillo M. et al., 2017, *MNRAS*, 471, 4398
- Pier E. A., Krolik J. H., 1992, *ApJ*, 399, L23
- Polimera M. S. et al., 2022, *ApJ*, 931, 44
- Proga D., Stone J. M., Kallman T. R., 2000, *ApJ*, 543, 686
- Ricci C. et al., 2017, *Nature*, 549, 488
- Risaliti G., Elvis M., Nicastro F., 2002, *ApJ*, 571, 234
- Risaliti G., Elvis M., Fabbiano G., Baldi A., Zezas A., 2005, *ApJ*, 623, L93
- Ross N. P., Graham M. J., Calderone G., Ford K. S., McKernan B., Stern D., 2020, *MNRAS*, 498, 2339
- Roth N., Kasen D., Hopkins P. F., Quataert E., 2012, *ApJ*, 759, 36
- Ruan J. J. et al., 2016, *ApJ*, 826, 188
- Runnoe J. C. et al., 2016, *MNRAS*, 455, 1691
- Salpeter E., 1977, *ARA&A*, 15, 267
- Sanders D. B., Soifer B. T., Elias J. H., Madore B. F., Matthews K., Neugebauer G., Scoville N. Z., 1988, *ApJ*, 325, 74
- Sanfrutos M., Miniutti G., Dovčiak M., Agís-González B., 2016, *Astron. Nachr.*, 337, 546
- Savage B. D., Mathis J. S., 1979, *ARA&A*, 17, 73
- Seligman D., Hopkins P. F., Squire J., 2019a, *MNRAS*, 485, 3991
- Shen X., Hopkins P. F., Faucher-Giguère C.-A., Alexander D. M., Richards G. T., Ross N. P., Hickox R. C., 2020, *MNRAS*, 495, 3252
- Simm T., Salvato M., Saglia R., Ponti G., Lanzuisi G., Trakhtenbrot B., Nandra K., Bender R., 2016, *A&A*, 585, A129
- Simpson C., 2005, *MNRAS*, 360, 565
- Smith R., Vaughan S., 2007, *MNRAS*, 375, 1479
- Smith K. L., Mushotzky R. F., Boyd P. T., Malkan M., Howell S. B., Gelino D. M., 2018, *ApJ*, 857, 141
- Spitzer Jr L., 2008, *Physical Processes in the Interstellar Medium*, John Wiley and Sons, New York
- Squire J., Hopkins P. F., 2018a, *MNRAS*, 477, 5011
- Squire J., Hopkins P. F., 2018b, *ApJ*, 856, L15
- Squire J., Moroianu S., Hopkins P. F., 2022, *MNRAS*, 510, 110
- Stalewski M., Fritz J., Baes M., Nakos T., Popović L. Č., 2012, *MNRAS*, 420, 2756

- Steinwandel U. P., Kurov A. A., Hopkins P. F., Squire J., 2022, *MNRAS*, 515, 4797
- Stern D. et al., 2018, *ApJ*, 864, 27
- Stone Z. et al., 2022, *MNRAS*, 514, 164
- Storchi-Bergmann T., Schmitt H. R., Calzetti D., Kinney A. L., 1998, *AJ*, 115, 909
- Sturm E., Rigopoulou D., Spoon H., Moorwood A., Lutz D., Genzel R., 2006, *ApJ*, 653, L13
- Su K.-Y., Hopkins P. F., Hayward C. C., Faucher-Giguère C.-A., Kereš D., Ma X., Robles V. H., 2017, *MNRAS*, 471, 144
- Suberlak K. L., Ivezić Ž., MacLeod C., 2021, *ApJ*, 907, 96
- Suganuma M. et al., 2006, *ApJ*, 639, 46
- Thompson T. A., Quataert E., Murray N., 2005, *ApJ*, 630, 167
- Thompson T. A., Fabian A. C., Quataert E., Murray N., 2015, *MNRAS*, 449, 147
- Tielens A. G. G. M., 2005, *The Physics and Chemistry of the Interstellar Medium*. Cambridge Univ. Press, Cambridge, UK
- Trakhtenbrot B. et al., 2019, *ApJ*, 883, 94
- Tristram K. et al., 2007, *A&A*, 474, 837
- Tristram K. R. W. et al., 2009a, *A&A*, 502, 67
- Tristram K. R. et al., 2009b, *A&A*, 502, 67
- Tsang B. T.-H., Milosavljević M., 2015, *MNRAS*, 453, 1108
- Übler H., Maiolino R., Curtis-Lake E., Pérez-González P. G., Curti M., Perna M., S. Arribas, S. Charlot, M.A. Marshall, D'Eugenio F., Scholtz J., 2023, arXiv preprint, arXiv: 2302.06647.
- Urry C. M., Padovani P., 1995, *PASP*, 107, 803
- Uttley P., McHardy I. M., 2004, *Prog. Theor. Phys. Suppl.*, 155, 170
- Venanzi M., Hönig S., Williamson D., 2020, *ApJ*, 900, 174
- Wada K., 2012, *ApJ*, 758, 66
- Wada K., Papadopoulos P. P., Spaans M., 2009, *ApJ*, 702, 63
- Wang J., Xu D., Wei J., 2018, *ApJ*, 858, 49
- Watanabe N., Kouchi A., 2008, *Prog. Surf. Sci.*, 83, 439
- Weingartner J. C., Draine B. T., 2001a, *ApJS*, 134, 263
- Weingartner J. C., Draine B., 2001b, *ApJ*, 563, 842
- Whittet D., Millar T., Williams D., 1993, *Dust and Chemistry in Astronomy*, IoP Publishing, Bristol, p. 9
- Wise J. H., Abel T., Turk M. J., Norman M. L., Smith B. D., 2012, *MNRAS*, 427, 311
- Yang Q. et al., 2018, *ApJ*, 862, 109

APPENDIX A: LIST OF SIMULATIONS

Table A1. Initial conditions for all simulations. The simulations organized by the gas column density, and the dashed lines separate simulations using the uniform flux approximation from the RDMHD runs. Columns show: (1) Simulation name. (2) Physical column density of the gas: N_{gas} . (3) Physical size of the largest grains: ϵ_{grain} . (4) Grain charge parameter $\tilde{\phi}_m \equiv 3 Z_{\text{grain}}^0 [e_{\text{grain}}^{\text{max}}] e / (4\pi c (\epsilon_{\text{grain}}^{\text{max}})^2 \rho_{\text{base}}^{1/2})$ of the largest grains. (5) Grain size parameter $\tilde{\alpha}_m \equiv (\tilde{\rho}_{\text{grain}}^i \epsilon_{\text{grain}}^{\text{max}}) / (\rho_{\text{base}} H_{\text{gas}})$ of the largest grains. (6) Gravity parameter $\tilde{g} \equiv |g| H_{\text{gas}} / c_s^2$. (7) Dust acceleration parameter: $\tilde{a}_d \equiv (3/4) (F_0 \langle Q \rangle_{\text{ext}} / c) / (\rho_{\text{base}} c_s^2)$. (8) Initial plasma $\beta_0 \equiv (c_s / v_A^0)^2$. (9) Notes for each run and key differences relative to its corresponding default run.

Name	$N_{\text{H}}[\text{cm}^{-2}]$	$\epsilon_{\text{grain}}^{\text{max}}[\mu\text{m}]$	$\tilde{\alpha}_m$	$\tilde{\phi}_m$	$\tilde{g}[10^5]$	$\tilde{a}_d[10^9]$	β^0	Notes
n1e22_eps1	1e + 22	1	6.5e-3	27.0	5.7	0.11	0.13	default
n1e22_eps0.1		0.1	6.5e-4	270.0	5.7	1.1	0.13	10x smaller $\epsilon_{\text{grain}}^{\text{max}}$
n1e22_eps0.01		0.01	6.5e-5	2700.0	5.7	11.0	0.13	100x smaller $\epsilon_{\text{grain}}^{\text{max}}$
n1e22_eps1_rhd		1	1e-2	10	1	0.05	1	default RDMHD
n1e22_eps1_rhd_c		1	1e-2	10	1	0.05	1	RDMHD – no RSOL ($\tilde{c} = c$)
n1e22_eps1_rhd_hr		1	1e-2	10	1	0.05	1	RDMHD – higher spatial resolution
n1e22_eps1_rhd_modB		1	6.5e-3	27.0	5.7	0.11	0.13	RDMHD – weaker \mathbf{B}^0
n1e22_eps1_rhd_modB_lr		1	6.5e-3	27.0	5.7	0.11	0.13	RDMHD – weaker \mathbf{B}^0 and lower spatial resolution
<hr/>								
n1e24_eps1	1e + 24	1	6.5e-5	2.7	5.7	0.11	0.13	default
n1e24_eps0.1		0.1	6.5e-6	27.0	5.7	1.1	0.13	10x smaller $\epsilon_{\text{grain}}^{\text{max}}$
n1e24_eps0.01		0.01	6.5e-7	270.0	5.7	11.0	0.13	100x smaller $\epsilon_{\text{grain}}^{\text{max}}$
n1e24_eps0.01_hr_t		0.01	6.5e-7	270.0	5.7	11.0	0.13	higher temporal resolution
n1e24_eps0.01_lr		0.01	6.5e-7	270.0	5.7	11.0	0.13	lower spatial resolution
n1e24_eps0.01_xlr		0.01	6.5e-7	270.0	5.7	11.0	0.13	much lower spatial resolution
n1e24_eps1_rhd		1	1e-4	1	1	0.05	1	default RDMHD
n1e24_eps1_rhd_c		1	1e-4	1	1	0.05	1	No RSOL ($\tilde{c} = c$)
n1e24_eps1_rhd_fw		1	6.5e-4	2.7	5.7	0.02	1	lower F_{rad} and stronger \mathbf{g}
n1e25_eps1	1e + 25	1	6.5e-6	0.85	5.7	0.11	0.13	default
n1e25_eps0.1		0.1	6.5e-7	8.5	5.7	1.1	0.13	10x smaller $\epsilon_{\text{grain}}^{\text{max}}$
n1e25_eps0.01		0.01	6.5e-8	85.0	5.7	11.0	0.13	100x smaller $\epsilon_{\text{grain}}^{\text{max}}$
n1e25_eps1_rhd		1	1e-5	0.32	1	0.05	1	default RDMHD
n1e25_eps1_rhd_fw		1	6.5e-6	0.85	5.7	0.02	0.13	lower F_{rad} and stronger \mathbf{g}
<hr/>								
n1e26_eps1	1e + 26	1	6.5e-7	0.27	5.7	0.11	0.13	default
n1e26_eps0.1		0.1	6.5e-8	2.7	5.7	1.1	0.13	10x smaller $\epsilon_{\text{grain}}^{\text{max}}$
n1e26_eps0.01		0.01	6.5e-9	27.0	5.7	11.0	0.13	100x smaller $\epsilon_{\text{grain}}^{\text{max}}$
n1e26_eps1_rhd_c		1	1e-6	0.1	1	0.05	1	default RDMHD
n1e26_eps1_rhd_hr		1	1e-6	0.1	1	0.05	1	RDMHD – higher spatial resolution
n1e26_eps1_rhd		1	1e-6	0.1	1	0.05	1	RDMHD – higher spatial resolution and RSOL
n1e26_eps1_rhd_modB		1	6.5e-7	0.27	5.7	0.11	0.13	weaker \mathbf{B}^0

This paper has been typeset from a $\text{\TeX}/\text{\LaTeX}$ file prepared by the author.